

SHEP-06-35

DCP-07-04

LPT-ORSAY-07-98

February 2, 2008

Charged Higgs boson phenomenology in Supersymmetric models with Higgs triplets

J. L. Díaz-Cruz,^{1,*} J. Hernández-Sánchez,^{2,†} S. Moretti,^{3,‡} and A. Rosado^{4,§}

¹*Fac. de Cs. Físico-Matemáticas, BUAP. Apdo. Postal 1364, C.P. 72000 Puebla, Pue., México and Dual C-P Institute of High Energy Physics, México.*

²*Centro de Investigación en Matemáticas, UAEH, Carr. Pachuca-Tulancingo Km. 4.5, C.P. 42184, Pachuca, Hgo., México and Dual C-P Institute of High Energy Physics.*

³*School of Physics and Astronomy, University of Southampton, Highfield, Southampton SO17 1BJ, UK and*

Laboratoire de Physique Théorique, U. Paris-Sud and CNRS, F-91405 Orsay, France.

⁴*Instituto de Física, BUAP. Apdo. Postal J-48, C.P. 72570 Puebla, Pue., México.*

(Dated: February 2, 2008)

We present a detailed study of the Higgs sector within an extension of the Minimal Supersymmetric Standard Model that includes one Complex Higgs Triplet (MSSM+1CHT). The model spectrum includes three singly charged Higgs bosons as well as three CP-even (or scalar) and two CP-odd (or pseudoscalar) neutral Higgs bosons. We present an approximated calculation of the one-loop radiative corrections to the neutral CP-even Higgs masses ($m_{H_i^0}$) and the couplings $H_i^0 Z^0 Z^0$ ($i = 1, 2, 3$), which determine the magnitude of the Higgs-strahlung processes $e^+e^- \rightarrow Z^0 H_i^0$. Limits from LEP2 are then considered, in order to obtain bounds on the neutral Higgs sector. Further, we also include the experimental limits from LEP2 on $e^+e^- \rightarrow H^+H^-$ and those on $\text{BR}(t \rightarrow b H^+)$ from Tevatron, to derive bounds on the mass of the two lightest charged Higgs bosons (H_1^\pm and H_2^\pm). Concerning the latter, we find some cases, where $m_{H_1^\pm} \simeq 90$ GeV, that are not excluded by any experimental bound, even for large values of $\tan \beta$, so that they should be looked for at the Large Hadron Collider (LHC).

PACS numbers: 12.60.Cn, 12.60.Fr, 11.30.Er

*Electronic address: jldiaz@cfm.buap.mx

I. INTRODUCTION

The Higgs spectrum of many well motivated extensions of the Standard Model (SM) often include charged Higgs bosons whose detection at future colliders would constitute a clear evidence of a Higgs sector beyond that of the Standard Model (SM) [1]. In particular, the 2-Higgs-Doublet-Model (2HDM, hereafter, of Type II), in both its Supersymmetric (SUSY) and non-SUSY versions [2], has been extensively studied as a prototype of a Higgs sector that includes one charged Higgs boson pair (H^\pm), whose detection is expected to take place at the LHC [3]. However, a definitive test of the mechanism of Electro-Weak Symmetry Breaking (EWSB) will require further studies aiming at pinning down the underlying complete Higgs spectrum. In particular, probing the properties of charged Higgs bosons could help to find out whether they are indeed associated with a weakly-interacting theory, as in the case of the most popular SUSY extension of the SM, the so-called Minimal Supersymmetric Standard Model (MSSM) [4], or with a strongly-interacting scenario, like the ones discussed recently [5]. Ultimately, while many analyses in this direction can be carried out at the LHC, it will be a future International Linear Collider (ILC) saying the definite word about which mechanism leads to mass generation. Notice that these tests should also allow one to probe the symmetries of the Higgs potential and to determine whether the charged Higgs bosons belong to a weak doublet or to some larger multiplet. Among the latter, in particular, Higgs triplets have been considered [6], mainly to search for possible manifestations of an explicit breaking of the custodial $SU(2)_c$ symmetry, which keeps Veltman's so-called 'rho parameter' close to one, i.e. $\rho \simeq 1$. Motivations to discuss Higgs triplets can also be drawn from models of neutrino masses [7] as well as scenarios with extra spacial dimensions [8]. Though most of the work has been within non-SUSY models [9], there have also been studies of SUSY scenarios with complex Higgs triplets, such as in [10], where some phenomenological aspects of the Higgs sector were explored. Subsequent work in this model has been done in [11].

Decays of charged Higgs bosons have been studied in the literature [12], including the radiative modes $W^\pm\gamma, W^\pm Z^0$ [13], mostly within the context of the 2HDM or its MSSM incarnation (including into SUSY particles [14]), but also for the effective Lagrangian extension of the 2HDM defined in [15] and more recently within an extension of the MSSM with one Complex Higgs Triplet (MSSM+1CHT) [16]. All these activities are particularly relevant especially in view of the fact

[†]Electronic address: jaimeh@uaeh.edu.mx

[‡]Electronic address: stefano@hep.phys.soton.ac.uk

[§]Electronic address: rosado@sirio.ifuap.buap.mx

that charged Higgs boson decays can be exploited to determine key parameters of the underlying Higgs sector [17]. Charged Higgs boson production at hadron colliders was studied long ago [18] and, more recently, systematic calculations of production processes at the upcoming LHC have been presented [19], including some higher order effects in QCD and SUSY QCD [20]. Current bounds on the mass of the charged Higgs bosons have been obtained at Tevatron, by studying the top decay $t \rightarrow b H^+$, which already eliminates some regions of the 2HDM and MSSM parameter spaces [21], whereas LEP2 gives a model independent bound of $m_{H^\pm} > 80$ GeV [22, 23].

In this paper we present a detailed study of the spectrum and discuss the phenomenology of the Higgs sector of the MSSM+1CHT model, i.e., the scenario that includes one complex Higgs triplet in addition to the usual MSSM Higgs content, namely two Higgs doublets. Our main focus will eventually be on the production and decay phenomenology of the charged Higgs states of the model.

This article is organized as follows. In section II, we discuss the Higgs sector of this model, in particular, we present the charged Higgs boson spectrum and the inclusion of an estimated calculation of the one-loop radiative corrections for the CP-even neutral Higgs sector. In this section, we also present a study of the couplings $H_i^0 Z^0 Z^0$, which are modified by radiative corrections. Then, in section III, we derive the expressions for the vertex $H^\pm f f'$ (where f and f' are generic fermions with cumulative electromagnetic charge ± 1) and we calculate the decay $t \rightarrow H_i^+ b$ in the framework of the MSSM+1CHT model, also presenting numerical results for the most relevant charged Higgs Branching Ratios (BR's)¹. (A comparison with latest bounds from Tevatron Run2 is also given therein.) A discussion of the main production mechanism at the LHC is presented in section IV. LHC event rates are given in section V. Finally, we summarize and conclude in section VI.

II. THE CHARGED HIGGS SPECTRUM IN A SUSY MODEL WITH AN ADDITIONAL COMPLEX HIGGS TRIPLET

The SUSY model with two doublets and a complex Higgs triplet (MSSM+1CHT) of [10] is one of the simplest extensions of the MSSM that allows one to study phenomenological consequences of an explicit breaking of the custodial $SU(2)_c$ symmetry [10, 11]. In the reminder of this section, we recap its main theoretical features.

¹ In the framework of the MSSM+1CHT the three charged Higgs states are denoted by H_i^\pm with the convention: $m_{H_1^\pm} < m_{H_2^\pm} < m_{H_3^\pm}$.

A. The Higgs potential of the model

The MSSM+1CHT model includes two Higgs doublets and a complex Higgs triplet given by

$$\Phi_1 = \begin{pmatrix} \phi_1^0 \\ \phi_1^- \end{pmatrix}, \quad \Phi_2 = \begin{pmatrix} \phi_2^+ \\ \phi_2^0 \end{pmatrix}, \quad \Sigma = \begin{pmatrix} \sqrt{\frac{1}{2}}\xi^0 & -\xi_2^+ \\ \xi_1^- & -\sqrt{\frac{1}{2}}\xi^0 \end{pmatrix}. \quad (1)$$

The Higgs triplet, of zero hypercharge, is described in terms of a 2×2 matrix representation: ξ^0 is the complex neutral field and ξ_1^- , ξ_2^+ denote the charged fields. The most general gauge invariant and renormalizable Superpotential that can be written for the Higgs Superfields $\Phi_{1,2}$ and Σ is given by:

$$W = \lambda \Phi_1 \cdot \Sigma \Phi_2 + \mu_1 \Phi_1 \cdot \Phi_2 + \mu_2 \text{Tr}(\Sigma^2), \quad (2)$$

where we have used the notation $\Phi_1 \cdot \Phi_2 \equiv \epsilon_{ab} \Phi_1^a \Phi_2^b$. The resulting scalar potential involving only the Higgs fields is thus written as

$$V = V_{SB} + V_F + V_D,$$

where V_{SB} denotes the most general soft-Supersymmetry breaking potential, which is given by

$$\begin{aligned} V_{SB} = & m_1^2 |\Phi_1|^2 + m_2^2 |\Phi_2|^2 + m_3^2 \text{Tr}(\Sigma^\dagger \Sigma) \\ & + [A \lambda \Phi_1 \cdot \Sigma \Phi_2 + B_1 \mu_1 \Phi_1 \cdot \Phi_2 + B_2 \mu_2 \text{Tr}(\Sigma^2) + h.c.], \end{aligned} \quad (3)$$

V_F is the SUSY potential from F-terms

$$\begin{aligned} V_F = & \left| \mu_1 \phi_2^0 + \lambda \left(\phi_2^+ \xi_1^- - \frac{1}{\sqrt{2}} \phi_2^0 \xi^0 \right) \right|^2 + \left| \mu_1 \phi_1^0 + \lambda \left(\phi_1^- \xi_2^+ - \frac{1}{\sqrt{2}} \phi_1^0 \xi^0 \right) \right|^2 \\ & + \left| \mu_1 \phi_2^+ + \lambda \left(\frac{1}{\sqrt{2}} \phi_2^+ \xi^0 - \phi_2^0 \xi_2^+ \right) \right|^2 + \left| \mu_1 \phi_1^- + \lambda \left(\frac{1}{\sqrt{2}} \phi_1^- \xi^0 - \phi_1^0 \xi_1^- \right) \right|^2 \\ & + \left| 2\mu_2 \xi^0 - \frac{\lambda}{\sqrt{2}} \left(\phi_1^0 \phi_2^0 + \phi_1^- \phi_2^+ \right) \right|^2 + \left| \lambda \phi_1^0 \phi_2^+ - 2\mu_2 \xi_2^+ \right|^2 + \left| \lambda \phi_1^- \phi_2^0 - 2\mu_2 \xi_1^- \right|^2, \end{aligned} \quad (4)$$

V_D is the SUSY potential from D-terms

$$\begin{aligned} V_D = & \frac{g^2}{8} \left[|\phi_1^0|^2 - |\phi_1^-|^2 + |\phi_2^+|^2 - |\phi_2^0|^2 + 2|\xi_2^+|^2 - 2|\xi_1^-|^2 \right]^2 \\ & + \frac{g'^2}{8} \left[|\phi_1^0|^2 + |\phi_1^-|^2 - |\phi_2^+|^2 - |\phi_2^0|^2 \right]^2 \\ & + \frac{g^2}{8} \left[\phi_1^{0*} \phi_1^- + \phi_2^{+*} \phi_2^0 + \sqrt{2}(\xi_2^+ + \xi_1^-) \xi^{0*} + h.c. \right]^2 \\ & - \frac{g^2}{8} \left[\phi_1^{-*} \phi_1^0 + \phi_2^{0*} \phi_2^+ + \sqrt{2}(\xi_2^+ - \xi_1^-) \xi^{0*} - h.c. \right]^2. \end{aligned} \quad (5)$$

In turn, the full scalar potential can be split into its neutral and charged parts, i.e., $V = V_{\text{charged}} + V_{\text{neutral}}$ [10, 11].

Besides the Supersymmetry-breaking mass terms, m_i^2 ($i = 1, 2, 3$), the potential depends on the parameters λ, μ_1, μ_2 , that appear in Eq. (2), as well as the trilinear and bilinear terms, A and B_i , respectively. For simplicity, we will assume that there is no CP violation in the Higgs sector and thus all the parameters and Vacuum Expectations Values (VEVs) are assumed to be real. In the charged Higgs sector with the basis of states $(\phi_2^+, \phi_1^{-*}, \xi_2^+, \xi_2^{-*})$ one has a 4×4 squared-matrix mass $(M_{\pm}^2)_{ij}$, $i = j = 1, \dots, 4$. For the CP-odd Higgs sector with the basis of states $(\frac{1}{\sqrt{2}}Im\phi_1^0, \frac{1}{\sqrt{2}}Im\phi_2^0, \frac{1}{\sqrt{2}}Im\xi^0)$ one obtains a 3×3 squared-matrix mass $(M_P^2)_{ij}$, $i = j = 1, 2, 3$. For the CP-even Higgs sector with the basis of states $(\frac{1}{\sqrt{2}}Re\phi_1^0, \frac{1}{\sqrt{2}}Re\phi_2^0, \frac{1}{\sqrt{2}}Re\xi^0)$ one also has a 3×3 squared-matrix mass $(M_S^2)_{ij}$, $i = j = 1, 2, 3$. The explicit expression of the resulting Higgs potential is given in Refs. [10, 11].

B. Parameters of the model and definition of scenarios

We can combine the VEVs of the doublet Higgs fields through the relation $v_D^2 \equiv v_1^2 + v_2^2$ and define $\tan\beta \equiv v_2/v_1$. Furthermore, the parameters v_D, v_T, m_W^2 and m_Z^2 are related as follows:

$$\begin{aligned} m_W^2 &= \frac{1}{2}g^2(v_D^2 + 4v_T^2), \\ m_Z^2 &= \frac{\frac{1}{2}g^2v_D^2}{\cos^2\theta_W}, \end{aligned}$$

which implies that the ρ -parameter is different from 1 at the tree level, namely,

$$\rho \equiv \frac{M_W^2}{M_Z^2 \cos^2\theta_W} = 1 + 4R^2, \quad R \equiv \frac{v_T}{v_D}. \quad (6)$$

The bound on R is obtained from the ρ parameter measurement, which presently lies in the range 0.9993–1.0006, from the global fit reported in Refs. [6, 23]. Thus, one has $R \leq 0.012$ and $v_T \leq 3$ GeV. We have taken into account this bound in our numerical analyses.

Thus, the Higgs sector of this model depends of the following parameters: (i) the gauge-related parameters $(g, g', v, R, \tan\beta)$; (ii) the Yukawa couplings (λ, μ_1, μ_2) and (iii) the soft Supersymmetry-breaking parameters (A, B_1, B_2) . The gauge-related parameters can be replaced by the quantities $(G_F, \alpha, m_W, \rho, \tan\beta)$. For the numerical analysis to be realized in the remainder of this paper, we must make sure that the following theoretical conditions of the MSSM+1CHT are satisfied: (a) the global stability condition of the potential; (b) the necessary condition for having a global minimum and (c) the positivity of the mass eigenvalues of the full spectrum of charged, pseudoscalar and scalar Higgs bosons [10].

The parameter space analyzed here for the MSSM+1CHT is the same that was considered before in the specialized literature [10, 16], namely, we consider characteristic values below their perturbative limits. Small and large values of $\tan\beta$ are both considered. Typical cases for A , B_1 , B_2 , μ_1 and μ_2 are used to define the following scenarios.

Scenario A. It is defined by considering $B_1 = \mu_1 = 0$, $B_2 = -A$ and $\mu_2 = 100$ GeV while for λ we shall consider the values $\lambda = 0.1, 0.5, 1.0$. In this scenario it happens that the additional Higgs triplet plays a significant role in EWSB.

Scenario B. This scenario is defined by choosing: $B_2 = \mu_2 = 0$, $B_1 = -A$, while for λ we shall consider again the values $\lambda = 0.1, 0.5, 1.0$. Most results will take $\mu_1 = 200$ GeV, though other values (such as $\mu_1 = 400, 700$ GeV) will also be considered. Here, the effects of the additional Higgs triplet are smaller, hence the behaviour of the model is similar to that of the MSSM.

C. One-loop radiative corrections to the CP-even Higgs bosons masses in the MSSM+1CHT

In some cases, within the Scenarios A and B, we will show that a very light CP-even Higgs boson appears at the tree level, with a mass around 10 GeV, which can even be as small as $\mathcal{O}(0.1)$ GeV. However, it is known that, in the MSSM, the inclusion of radiative corrections from top and stop loops can alter significantly the (lightest) neutral CP-even Higgs mass. Thus, we can expect that similar effects will appear here and, furthermore, one also needs to consider in the MSSM+1CHT a possible large correction from Higgs-chargino loops, which could lift the corresponding Higgs mass above current experimental bounds. This means that one needs to include all such radiative corrections in order to avoid misleading conclusions. We are also interested in discussing the neutral Higgs bosons masses here because of their possible appearance in charged Higgs boson decays. As it will be shown later, this effect is important for large regions of the MSSM+1CHT parameter space.

The radiative corrections to Supersymmetric Higgs boson masses can be evaluated using the effective potential technique [24], which at one-loop reads:

$$V_1(Q) = V_0(Q) + \Delta V_1(Q), \quad (7)$$

$$\Delta V_1(Q) = \frac{1}{64\pi^2} \text{Str} M^4 \left(\log \frac{M^2}{Q^2} - \frac{3}{2} \right), \quad (8)$$

where $V_0(Q)$ is the tree-level potential evaluated with couplings renormalized at some scale Q ,

Str denotes the conventional Supertrace and M^2 is the mass matrix for the CP-even sector. As discussed in [24], the radiatively-corrected Higgs mass-squared matrix is given by the matrix of the second derivatives of V_1 with respect to the Higgs fields, which is written as a function of their self-energies. In the MSSM, we know that the most important contributions to the Higgs self-energies at the one-loop level come from the diagrams with the top quark (and its scalar partner) circulating in the loop, due to the large top Yukawa coupling. However, for very large values of $\tan\beta$, the bottom-sbottom contributions can become non-negligible. Therefore, for our settings, the dominant contributions to the Supertrace in the MSSM+1CHT are due to the top-stop and bottom-sbottom loops. Within this approximation, it happens that the squared-mass matrix of the CP-even Higgs bosons only gets corrected along its (1, 1) and (2, 2) elements, given as follows:

$$\begin{aligned}(\Delta M_S^2)_{1,1} &= \frac{3}{8\pi^2} \lambda_b^2 m_b^2 \log \frac{m_b^4}{m_b^4}, \\(\Delta M_S^2)_{2,2} &= \frac{3}{8\pi^2} \lambda_t^2 m_t^2 \log \frac{m_t^4}{m_t^4},\end{aligned}\tag{9}$$

where $\lambda_{t,b}$ are the Yukawa couplings and the D-terms are omitted. In short, in the MSSM+1CHT, the radiative corrections to the Higgs boson masses must include the dominant contribution from the top-stop and bottom-sbottom systems. For this, it is enough to suitably modify the elements $(\Delta M_S^2)_{1,1}$, $(\Delta M_S^2)_{2,2}$ to the squared-mass matrix M_S^2 of the CP-even Higgs boson. Furthermore, as intimated already, we must also evaluate the contribution from the fermionic partner of the Higgs Superfields, which includes the Higgs-Higgsino triplets, because there is a potentially large effect emerging in the calculation of the squared-mass matrix of the CP-even Higgs bosons when the parameter λ is large. Similarly to the top-stop and bottom-sbottom corrections, we estimate that the correction from the Higgs-Higgsino only modifies the element $(M_S^2)_{3,3}$

$$(\Delta M_S^2)_{3,3} = \frac{3}{8\pi^2} \lambda^2 m_{\chi^\pm}^2 \log \frac{m_{\chi^\pm}^4}{m_{H^\pm}^4},\tag{10}$$

where λ is the Yukawa coupling that appears in the Superpotential of the Higgs Superfields and – within our approximation – we take m_{χ^\pm} and m_{H^\pm} as the mass scales of the lightest charginos and charged Higgs bosons, respectively, i.e., $m_{\chi^\pm} \simeq m_{\chi_1^\pm}$ and $m_{H^\pm} \simeq m_{H_1^\pm}$. D-terms are omitted, as well as possible effects from stop, sbottom and Higgsino mixing. Previous studies of Higgs mass bounds of this model were considered by J. R. Espinosa and M. Quirós [25], who concluded that the lightest Higgs boson of the model satisfy the bound,

$$m_{H_1^0} \lesssim m_Z \sqrt{\cos^2(2\beta) + 1/2(\lambda^2 v^2 / m_Z^2) \sin^2(2\beta)}.\tag{11}$$

Thus, for values of λ that are consistent with perturbativity, which then implies a bound of the order $m_{H_1^0} \lesssim 155$ GeV. Throughout this paper we take values of λ that do not saturate this bound. A more complete calculation of the radiative corrections at one-loop level for this model is in progress [26].

The main consequence of these radiative corrections is that the lightest CP-even Higgs mass can be enhanced at such levels that it makes it possible to pass current experimental bounds from LEP2. Besides, the radiative corrections affect mainly the neutral Higgs bosons sector, in particular the production of the neutral scalar Higgs in e^+e^- collisions, which is the Higgs-strahlung processes $e^+e^- \rightarrow H_i^0 Z^0$, whose cross sections can be expressed in terms of the SM Higgs boson (herein denoted by ϕ_{SM}^0) production formula and the Higgs- $Z^0 Z^0$ coupling, as follows [27]:

$$\begin{aligned} \sigma_{H_i^0 Z} &= R_{H_i^0 Z^0 Z^0}^2 \sigma_{H_i^0 Z}^{SM}, \\ R_{H_i^0 Z^0 Z^0}^2 &= \frac{g_{H_i^0 Z^0 Z^0}^2}{g_{\phi_{SM}^0 Z^0 Z^0}^2}, \end{aligned} \quad (12)$$

where $g_{H_i^0 Z^0 Z^0}^2$ is the coupling $H_i^0 Z^0 Z^0$ in the MSSM+1CHT and $g_{\phi_{SM}^0 Z^0 Z^0}^2$ is the SM coupling $\phi_{SM}^0 Z^0 Z^0$, which obey the relation

$$\sum_{i=1}^3 g_{H_i^0 Z^0 Z^0}^2 = g_{\phi_{SM}^0 Z^0 Z^0}^2. \quad (13)$$

In particular, for our model the factor $R_{H_i^0 Z^0 Z^0}^2$ is given by:

$$R_{H_i^0 Z^0 Z^0}^2 = (V_{1i}^S c_\beta + V_{2i}^S s_\beta)^2, \quad (14)$$

where V_{ij}^S denote the ij -elements of the rotation matrix for the CP-even neutral sector, which relates the physical states H_i^0 and the real part of the fields $\phi_1^0, \phi_2^0, \xi^0$ in the following way:

$$\begin{pmatrix} \frac{1}{\sqrt{2}}\phi_1^0 \\ \frac{1}{\sqrt{2}}\phi_2^0 \\ \frac{1}{\sqrt{2}}\xi^0 \end{pmatrix} = \begin{pmatrix} V_{11}^S & V_{12}^S & V_{13}^S \\ V_{21}^S & V_{22}^S & V_{23}^S \\ V_{31}^S & V_{32}^S & V_{33}^S \end{pmatrix} \begin{pmatrix} H_1^0 \\ H_2^0 \\ H_3^0 \end{pmatrix}, \quad (15)$$

where the V_{ij}^S are modified by the one-loop radiative corrections to the CP-even sector of our model. For our numerical analysis of the Higgs mass spectrum in the MSSM+1CHT we consider the experimental limits on the charged Higgs mass from LEP2 and apply it to the lightest charged Higgs state H_1^\pm [22, 23]. The bounds on the neutral Higgs bosons H_1^0, H_2^0 are expressed in terms of the LEP2 bounds for $R_{H_i^0 Z^0 Z^0}^2$ [27]. We will show that this excludes large regions of the parameter space of the MSSM+1CHT model. This is summarized in Tables I–IV. Herein, we define as the

“marginal regions” those cases that almost pass LEP2 bounds on the neutral Higgs, i.e., when $m_{H_{1,2}^0} \sim 110$ GeV and/or $R_{H_{1,2}^0 Z^0 Z^0}^2$ are not consistent with experimental bounds but for which we expect that the complete calculation of the one-loop radiative corrections to the mass of the neutral Higgs boson in question could enhance its mass, thereby allowing it to eventually pass said experimental limits.

D. Higgs masses: numerical results

Let us consider first Scenario A. Figures 1, 2 and 3(4, 5 and 6) show the results for charged(neutral) Higgs bosons masses as a function of $\tan\beta$, in the range $1 \leq \tan\beta \leq 100$, for the cases $\lambda = 0.1, 0.5, 1.0$, while taking $A = 200, 300, 400$ GeV, respectively. Throughout this paper we shall assume that the numerical values for stop and sbottom masses, taken at the electroweak scale, are degenerated. The above results for charged Higgs masses is based on the tree-level analysis. Similarly, the coming results for the pseudoscalar masses is also based on the tree-level formulae. However, the masses of the neutral CP-even Higgs bosons is based in the previous discussion of one-loop radiative corrections to the Higgs masses. For the stop, sbottom and chargino masses we take as input the value $m = 1$ TeV. In Figure 1 we present the charged Higgs boson masses for $\lambda = 0.1$. We can see that the lightest charged Higgs boson has a mass $m_{H_1^\pm} \lesssim m_{W^\pm}$, which is not below the theoretical limit that one obtains in the MSSM. Similarly, Figure 2 shows the charged Higgs boson masses for the case $\lambda = 0.5$, and again we have that $m_{H_1^\pm} \lesssim m_{W^\pm}$ is possible but only for large $\tan\beta$. Furthermore, here it is possible for both H_1^\pm and H_2^\pm to be lighter than the top quark. Figure 3 shows the charged Higgs boson masses for the case $\lambda = 1$: now the lightest charged Higgs boson has a mass in the range $100 \text{ GeV} < m_{H_1^\pm} < 200 \text{ GeV}$.

Figure 4 shows the neutral Higgs spectrum for the case $\lambda = 0.1$, and we notice the presence of a light CP-even Higgs boson with $11 \text{ GeV} < m_{H_1^0} < 50 \text{ GeV}$, especially for low values of $\tan\beta$ (≤ 5), that at first sight it would seem excluded by the LEP2 experimental limits. In fact, when one compares the results for $R_{H_1^0 Z^0 Z^0}^2$ obtained for this model, which measures the strength of the Higgs-strahlung process, with the LEP2 bounds [27], which require it to be less than 0.01, we conclude that this scenario is indeed excluded, as it is summarized in our Table I. We assume that the lightest neutral Higgs boson decays predominantly into $b\bar{b}$ mode. Similarly, Figure 5 considers the case $\lambda = 0.5$, and again we find $11 \text{ GeV} < m_{H_1^0} < 50 \text{ GeV}$ for $1 \leq \tan\beta \leq 100$. However, we find that, for $\tan\beta \leq 77$, $R_{H_1^0 Z^0 Z^0}^2$ is within the range allowed by LEP2. There is also a region where $111 \text{ GeV} < m_{H_2^0} < 114 \text{ GeV}$, which we identify as marginal. Finally, Figure 6 corresponds

to the case $\lambda = 1.0$, and we find that $14 \text{ GeV} < m_{H_1^0} < 89 \text{ GeV}$, for $15 \leq \tan \beta$ and, although $R_{H_1^0 Z^0 Z^0}^2 < 0.01$, again we find that this is a marginal region because $111 \text{ GeV} < m_{H_2^0} < 114 \text{ GeV}$.

As a lesson from these figures, for the case $\lambda = 0.5$, we find that the LEP2 limit on the charged Higgs mass allows cases where $m_{H_1^\pm} \lesssim m_{W^\pm}$, while the neutral Higgs bosons (chiefly H_1^0) satisfy the experimental limits of LEP2. However, the case $\lambda = 0.1$ is not a favorable scenario, because $R_{H_1^0 Z^0 Z^0}$ does not satisfy the experimental bounds. In contrast, for $\lambda = 1.0$, the charged Higgs boson masses are significantly heavier. A complete list of bounds for all cases considered within Scenario A is shown in Table I.

TABLE I: Analysis of $R_{H_i^0 Z^0 Z^0}^2$ consistent with LEP. We consider experimental limits allowed by LEP2 for charged and neutral Higgs bosons, for Scenario A with $A = 200, 300, 400 \text{ GeV}$ and $\mu_2 = 100 \text{ GeV}$.

$\lambda = 0.1$	$\tan \beta \leq 5$	$m_{H_1^\pm} \approx 81 \text{ GeV}$ $11 \text{ GeV} < m_{H_1^0} < 50 \text{ GeV}$ $111 \text{ GeV} < m_{H_2^0} < 118 \text{ GeV}$	$0.15 < R_{H_1^0 Z^0 Z^0}^2 < 0.8$ $R_{H_2^0 Z^0 Z^0}^2 < 0.8$	Excluded by $R_{H_1^0 Z^0 Z^0}^2$
$\lambda = 0.5$	$\tan \beta \leq 77$	$79.8 \text{ GeV} < m_{H_1^\pm} < 118 \text{ GeV}$ $12 \text{ GeV} < m_{H_1^0} < 50 \text{ GeV}$ $111 \text{ GeV} < m_{H_2^0} < 114 \text{ GeV}$	$0.002 < R_{H_1^0 Z^0 Z^0}^2 < 0.2$ $0.9 < R_{H_2^0 Z^0 Z^0}^2$	Allowed by $R_{H_1^0 Z^0 Z^0}^2$, but marginal for $R_{H_2^0 Z^0 Z^0}^2$
$\lambda = 1$	$15 \leq \tan \beta$	$89 \text{ GeV} < m_{H_1^\pm} < 187 \text{ GeV}$ $14 \text{ GeV} < m_{H_1^0} < 89 \text{ GeV}$ $111 \text{ GeV} < m_{H_2^0} < 114 \text{ GeV}$	$R_{H_1^0 Z^0 Z^0}^2 < 0.01$ $0.9 < R_{H_2^0 Z^0 Z^0}^2$	Allowed by $R_{H_1^0 Z^0 Z^0}^2$, but marginal for $R_{H_2^0 Z^0 Z^0}^2$

For Scenario B, Figures 7, 8 and 9(10, 11 and 12) show the charged(neutral) Higgs bosons masses, as a function of $\tan \beta$ in the range $1 \leq \tan \beta \leq 100$, and for the cases $\lambda = 0.1, 0.5, 1.0$, taking $A = 200, 300, 0.1 \text{ GeV}$, respectively. The lowest value ($A = 0.1$) is designed in order to get charged Higgs masses below the top mass. Let us comment first the results found for the charged Higgs mass in the case $\lambda = 0.1$, that appear in Figure 7. We can see that the lightest charged Higgs boson has a mass above 300 GeV for $A = 200, 300 \text{ GeV}$, while even for $A = 0.1 \text{ GeV}$, it has a mass above m_{W^\pm} , but it is still lighter than the top quark. Similarly, Figure 8 shows the charged Higgs boson masses for the case $\lambda = 0.5$. We find that, for $A = 200, 300 \text{ GeV}$, $m_{H_1^\pm} > 300 \text{ GeV}$, while, for $A = 0.1 \text{ GeV}$, the mass is still in the range $100 \text{ GeV} < m_{H_1^\pm} < m_t$. In turn, Figure 9 shows the charged Higgs boson masses for $\lambda = 1$. Now, we have that the lightest charged Higgs boson is heavier than the top quark, even for $A = 0.1 \text{ GeV}$.

Let us now discuss the neutral Higgs spectrum. Figure 10 shows the case $\lambda = 0.1$ for $A = 200, 300 \text{ GeV}$, where one finds that $60 \text{ GeV} < m_{H_1^0} < 110 \text{ GeV}$, for $1 \leq \tan \beta \leq 100$, but the region allowed by $R_{H_1^0 Z^0 Z^0}^2$ corresponds to $10 \leq \tan \beta$, while the parameter area corresponding to $m_{H_1^0} \sim 110 \text{ GeV}$ is of marginal type. Then, the case $A = 0.1 \text{ GeV}$ gives neutral Higgs masses within the

TABLE II: Analysis of $R_{H_1^0 Z^0 Z^0}^2$ consistent with LEP. We consider experimental limits by LEP2 for charged and neutral Higgs bosons, for Scenario B with $A = 200, 300$ GeV and $\mu_1 = 200$ GeV.

$\lambda = 0.1$	$10 \leq \tan \beta \leq 100$	$294 \text{ GeV} < m_{H_1^\pm} < 532 \text{ GeV}$ $m_{H_1^0} \approx 110 \text{ GeV}$ $300 \text{ GeV} < m_{H_2^0} < 538 \text{ GeV}$	$0.99 < R_{H_1^0 Z^0 Z^0}^2$ $R_{H_2^0 Z^0 Z^0}^2 < 0.001$	Marginally allowed by $R_{H_1^0 Z^0 Z^0}^2$
$\lambda = 0.5$	$1 \leq \tan \beta \leq 100$	$300 \text{ GeV} < m_{H_1^\pm} < 1200 \text{ GeV}$ $100 \text{ GeV} < m_{H_1^0} < 107 \text{ GeV}$ $290 \text{ GeV} < m_{H_2^0} < 1200 \text{ GeV}$	$0.99 < R_{H_1^0 Z^0 Z^0}^2$ $R_{H_2^0 Z^0 Z^0}^2 < 0.001$	Marginally allowed by $R_{H_1^0 Z^0 Z^0}^2$
$\lambda = 1$	$1 \leq \tan \beta \leq 100$	$340 \text{ GeV} < m_{H_1^\pm} < 1690 \text{ GeV}$ $104 \text{ GeV} < m_{H_1^0} < 176 \text{ GeV}$ $252 \text{ GeV} < m_{H_2^0} < 1700 \text{ GeV}$	$0.99 < R_{H_1^0 Z^0 Z^0}^2$ $R_{H_2^0 Z^0 Z^0}^2 < 0.001$	Allowed by $R_{H_1^0 Z^0 Z^0}^2$

range $14 \text{ GeV} < m_{H_1^0} < 50 \text{ GeV}$, $m_{H_2^0} \sim 110 \text{ GeV}$, for which one finds that $R_{H_1^0 Z^0 Z^0}^2 < 0.01$. In this case we have a marginally allowed region. Figure 11 corresponds to the case $\lambda = 0.5$, for $A = 200, 300$ GeV, and now we have $100 \text{ GeV} < m_{H_1^0} < 107 \text{ GeV}$ for $1 \leq \tan \beta \leq 100$. However, we find that $0.9 < R_{H_1^0 Z^0 Z^0}^2$, so that this region is marginal for $m_{H_1^0}$. For the case $A = 0.1$ GeV we have $16 \text{ GeV} < m_{H_1^0} < 50 \text{ GeV}$, $m_{H_2^0} \sim 107 \text{ GeV}$, but also $R_{H_1^0 Z^0 Z^0}^2 < 0.01$, as we can see in Table III. We consider that this is a marginally allowed region by LEP2. Furthermore, Figure 12 includes the case $\lambda = 1$, for $A = 200, 300$ GeV, and we find $104 \text{ GeV} < m_{H_1^0} < 176 \text{ GeV}$, with $0.9 < R_{H_1^0 Z^0 Z^0}^2$, again a marginal region allowed by LEP2, namely when $m_{H_1^0} < 115 \text{ GeV}$ and $10 \leq \tan \beta$. Finally, in the case $A = 0.1$ GeV, we have $14 \text{ GeV} < m_{H_1^0} < 46 \text{ GeV}$, $m_{H_2^0} \sim 104 \text{ GeV}$, and $R_{H_1^0 Z^0 Z^0}^2 < 0.01$, as we can see in Table III. We also identify this as a possible marginal region for LEP2 [27].

As a lesson from this second set of figures, we can state that, for the cases $\lambda = 0.1, 0.5, 1.0$, which leave the range $\tan \beta \geq 25$ and $A = 0.1$ as acceptable, we have $84 \text{ GeV} < m_{H^\pm} < 200 \text{ GeV}$, while the neutral Higgs bosons lay in the mass range disallowed by the experimental limits of LEP2. However, in the cases with $A = 200, 300$ GeV, we obtain masses of the charged Higgs boson heavier than the top quark. A complete list of bounds for all cases considered within Scenario B is shown in Tables II and III.

Finally, in order to consider possible variations with μ_1 and the behavior in the limit $A \rightarrow 0$, we present the charged Higgs boson masses as function of $\tan \beta$, in Figure 13, for $\lambda = 0.5$, $A = 0$ and for $\mu_1 = 200, 400, 700$ GeV. We can see that for all these cases $m_{H^\pm} \sim 130 \text{ GeV}$. The corresponding results for the neutral spectrum are shown in Figure 14 and in Table IV, which indicate the presence of two light neutral Higgs states, which lay in the range: $10 \text{ GeV} < m_{H_1^0} < 50 \text{ GeV}$, $97 \text{ GeV} < m_{H_2^0} < 107 \text{ GeV}$, for $2 \leq \tan \beta \leq 6$. In this case we also find $0.007 < R_{H_1^0 Z^0 Z^0}^2 < 0.06$,

TABLE III: Same analysis of Table II, but taking $A = 0.1$ GeV.

$\lambda = 0.1$	$12 \leq \tan \beta \leq 100$	$84 \text{ GeV} < m_{H_1^\pm} < 95 \text{ GeV}$ $14 \text{ GeV} < m_{H_1^0} < 50 \text{ GeV}$ $m_{H_2^0} \approx 110 \text{ GeV}$	$R_{H_1^0 Z^0 Z^0}^2 < 0.01$ $0.99 < R_{H_2^0 Z^0 Z^0}^2$	Allowed for $R_{H_1^0 Z^0 Z^0}^2$ Marginal region for $R_{H_2^0 Z^0 Z^0}^2$
$\lambda = 0.5$	$4 \leq \tan \beta \leq 100$	$121 \text{ GeV} < m_{H_1^\pm} < 129 \text{ GeV}$ $16 \text{ GeV} < m_{H_1^0} < 50 \text{ GeV}$ $m_{H_2^0} \approx 107 \text{ GeV}$	$R_{H_1^0 Z^0 Z^0}^2 < 0.01$ $0.98 < R_{H_2^0 Z^0 Z^0}^2$	Allowed for $R_{H_1^0 Z^0 Z^0}^2$ Marginal region for $R_{H_2^0 Z^0 Z^0}^2$
$\lambda = 1$	$27 \leq \tan \beta \leq 100$	$197 \text{ GeV} < m_{H_1^\pm} < 200 \text{ GeV}$ $14 \text{ GeV} < m_{H_1^0} < 46 \text{ GeV}$ $103 \text{ GeV} < m_{H_2^0} < 105 \text{ GeV}$	$R_{H_1^0 Z^0 Z^0}^2 < 0.01$ $0.99 < R_{H_2^0 Z^0 Z^0}^2$	Allowed for $R_{H_1^0 Z^0 Z^0}^2$ Marginal region for $R_{H_2^0 Z^0 Z^0}^2$

TABLE IV: Same analysis of Table II, but taking $A = 0$ GeV, $\mu_1 = 200, 400, 700$ GeV and $\lambda = 0.5$.

$\lambda = 0.5$	$1 < \tan \beta < 6$	$121 \text{ GeV} < m_{H_1^\pm} < 130 \text{ GeV}$ $10 \text{ GeV} < m_{H_1^0} < 50 \text{ GeV}$ $97 \text{ GeV} < m_{H_2^0} < 113 \text{ GeV}$	$0.006 < R_{H_1^0 Z^0 Z^0}^2 < 0.2$ $0.76 < R_{H_2^0 Z^0 Z^0}^2$	Allowed for $R_{H_1^0 Z^0 Z^0}^2$ Marginal region for $R_{H_2^0 Z^0 Z^0}^2$
-----------------	----------------------	--	---	--

which then gives a small region of $\tan \beta$ that could be allowed by the LEP2 data. In fact, for $\tan \beta \geq 6$, practically all these scenarios are ruled out by LEP2, because $m_{H_1^0} < 10$ GeV [27].

III. THE VERTEX $H^\pm f f'$ AND THE DECAY $t \rightarrow H_i^+ b$

In the two previous papers [11, 16], some of us have studied the bosonic interactions of the charged and neutral Higgs bosons, now we shall discuss the corresponding fermionic interactions and their implications for charged Higgs boson production through top quark decays and via Higgs-strahlung off-top quarks.

A. The Higgs boson coupling to fermions in the MSSM+1CHT

As in the MSSM, also in this model only the scalar doublets are coupled to the fermions, so that the Lagrangian of the Yukawa sector has the following expression:

$$\mathcal{L}_{Yuk} = -\lambda_u [\bar{u} P_L u \phi_2^0 - \bar{u} P_L d \phi_2^+] - \lambda_d [\bar{d} P_L d \phi_1^0 - \bar{d} P_L u \phi_1^-] + h.c., \quad (16)$$

where the parameters $\lambda_{u,d}$ are related to the fermion masses via

$$\lambda_u = \frac{\sqrt{2} m_u}{v_D s_\beta}, \quad \lambda_d = \frac{\sqrt{2} m_d}{v_D c_\beta}. \quad (17)$$

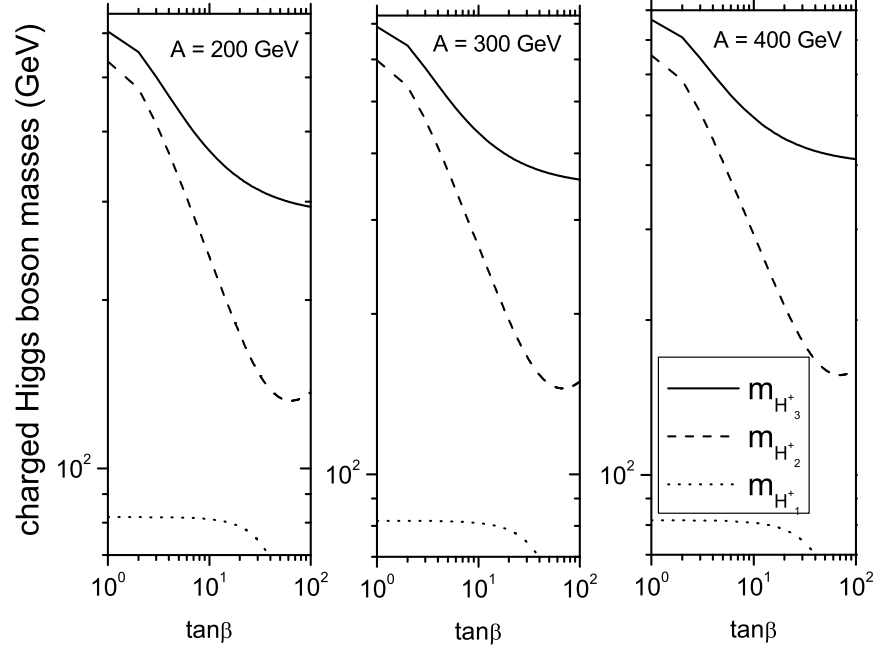


FIG. 1: Mass spectrum of the charged Higgs bosons, taking $\mu_2 = 100$ GeV and $\lambda = 0.1$, for: $A = 200$ GeV (left), $A = 300$ GeV (center), $A = 400$ GeV (right).

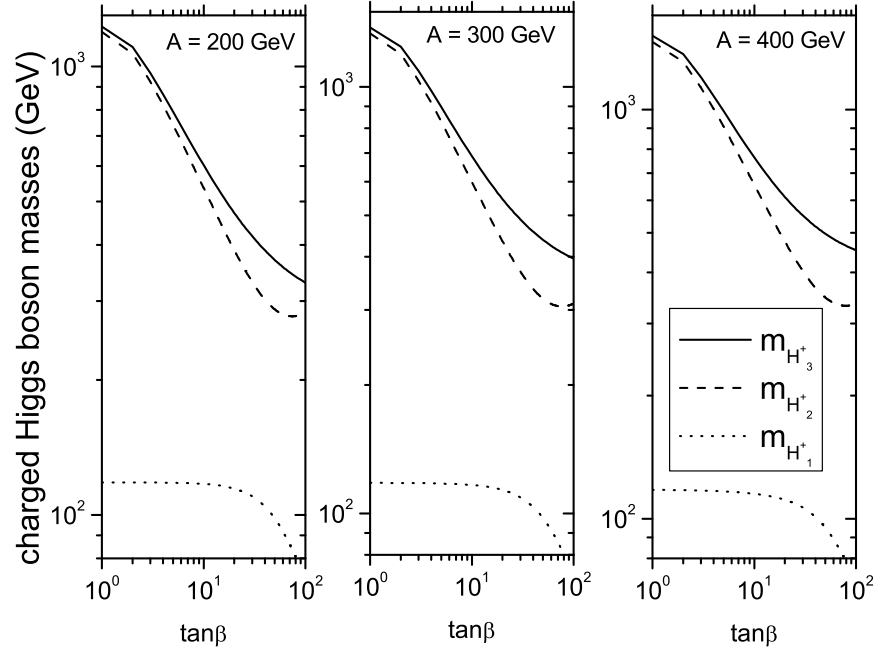


FIG. 2: Same as in Figure 1, but taking $\lambda = 0.5$.

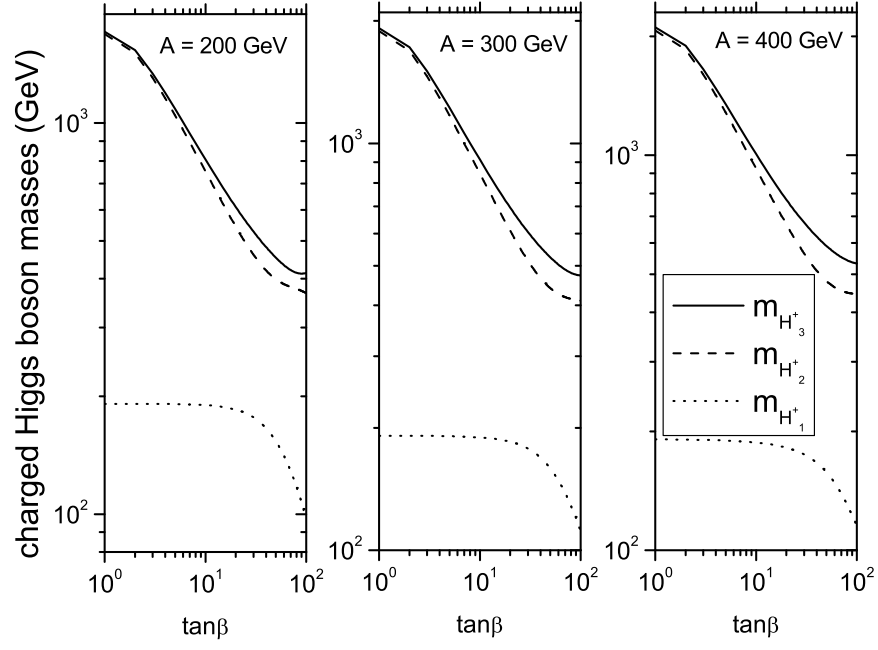


FIG. 3: Same as in Figure 1, but taking $\lambda = 1$.

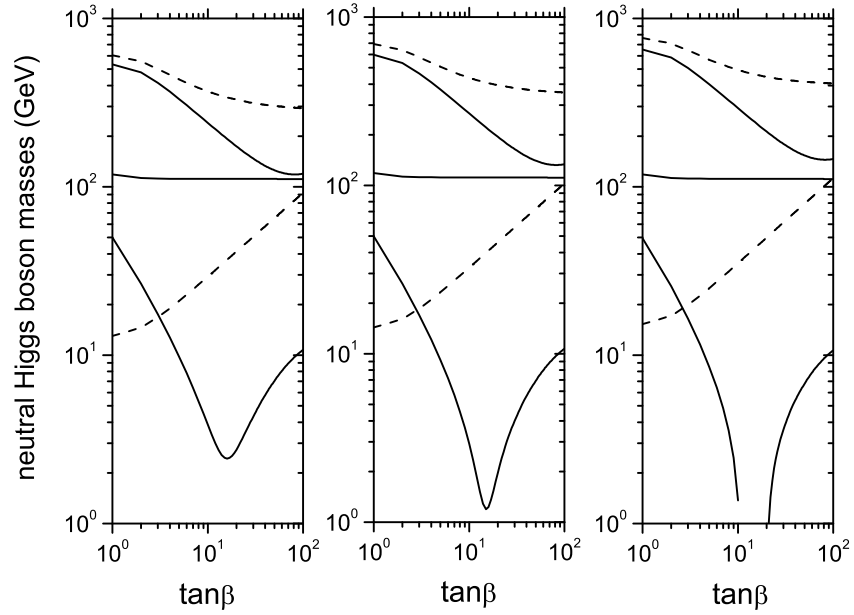


FIG. 4: Mass spectrum of the neutral Higgs bosons, taking $\mu_2 = 100$ GeV and $\lambda = 0.1$, for: $A = 200$ GeV (left), $A = 300$ GeV (center), $A = 400$ GeV (right). The solid lines correspond to scalar and the dashed lines to pseudoscalar eigenstates.

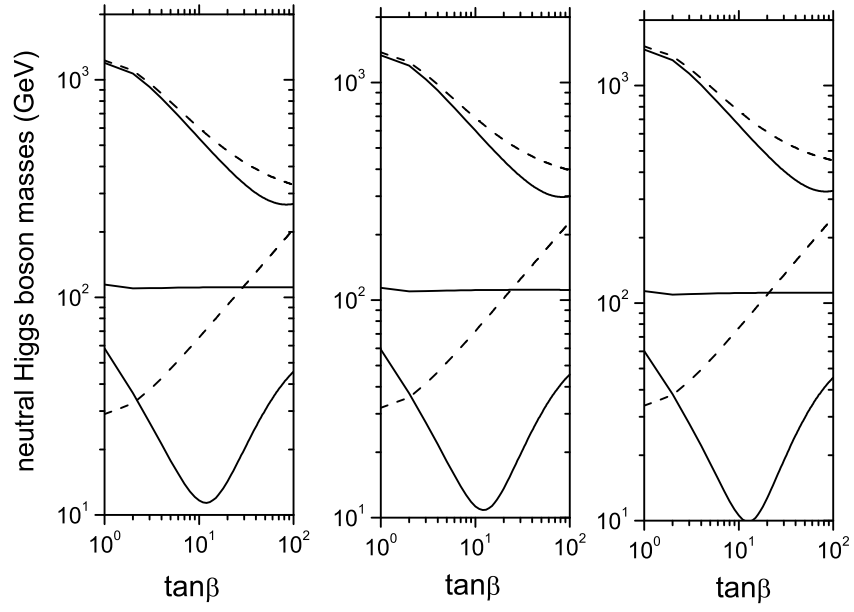


FIG. 5: Same as in Figure 4, but taking $\lambda = 0.5$.

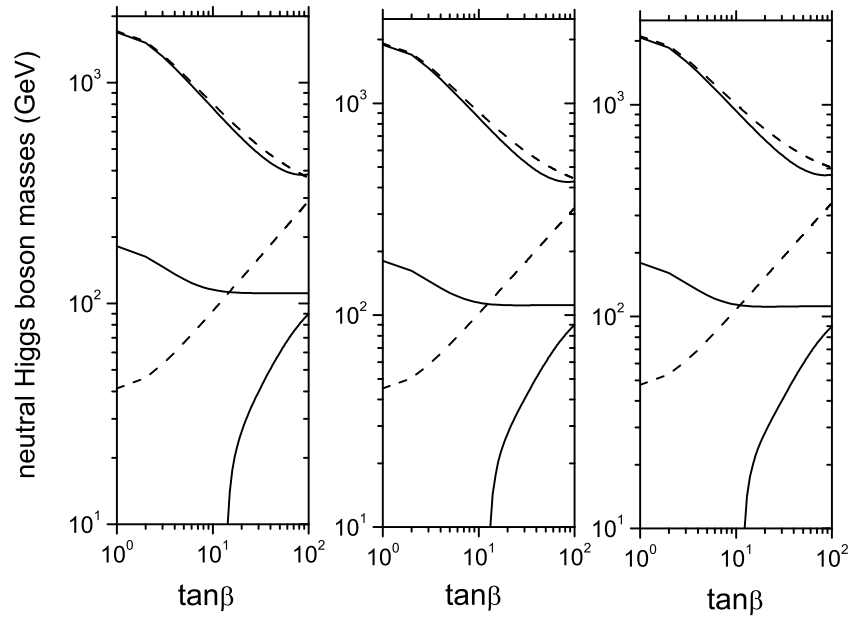


FIG. 6: Same as in Figure 4, but taking $\lambda = 1$.

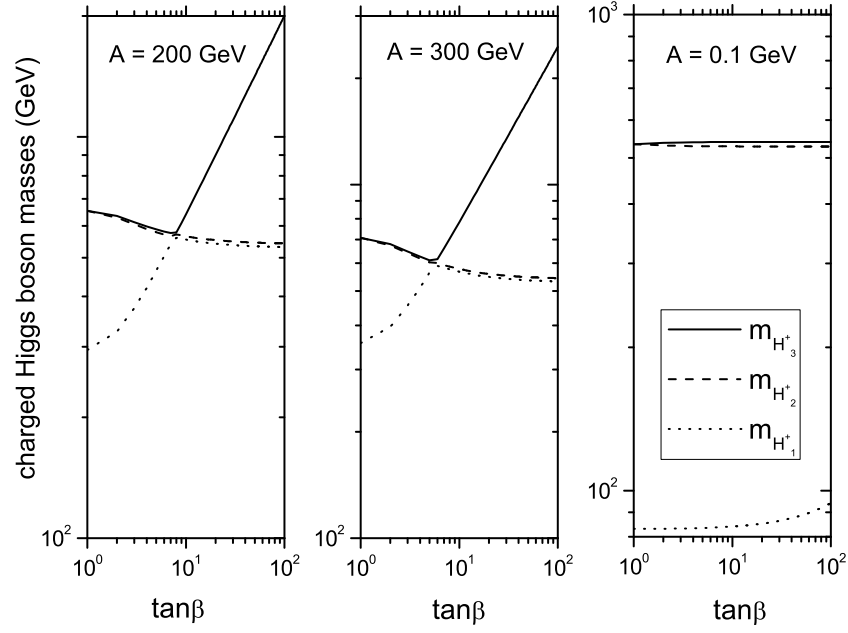


FIG. 7: Mass spectrum of the charged Higgs bosons, taking $\mu_1 = 200$ GeV and $\lambda = 0.1$, for: $A = 200$ GeV (left), $A = 300$ GeV (center), $A = 0.1$ GeV (right).

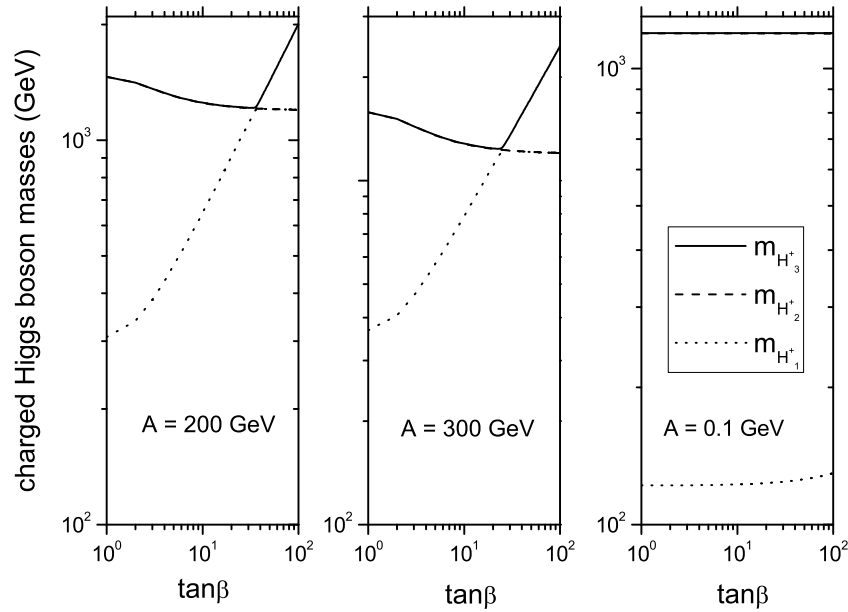


FIG. 8: Same as in Figure 7, but taking $\lambda = 0.5$.

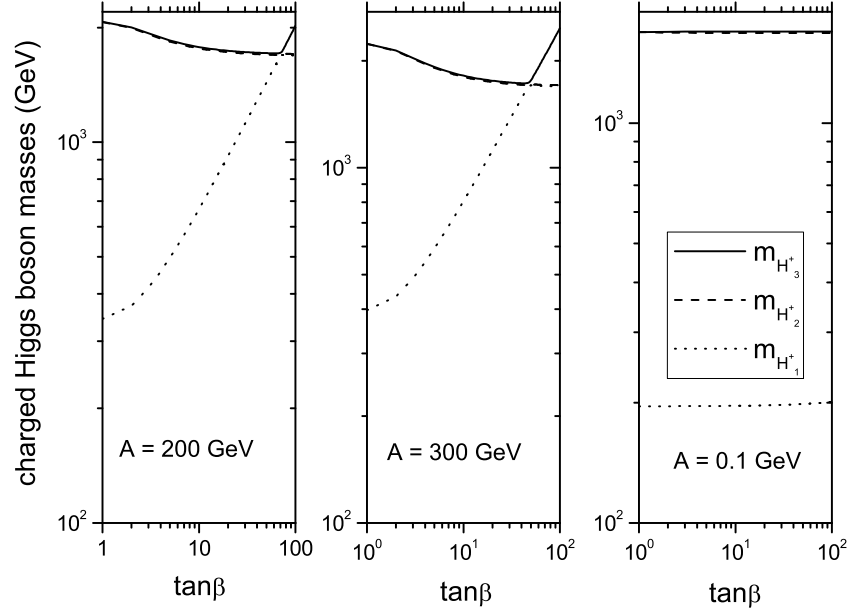


FIG. 9: Same as in Figure 7, but taking $\lambda = 1$.

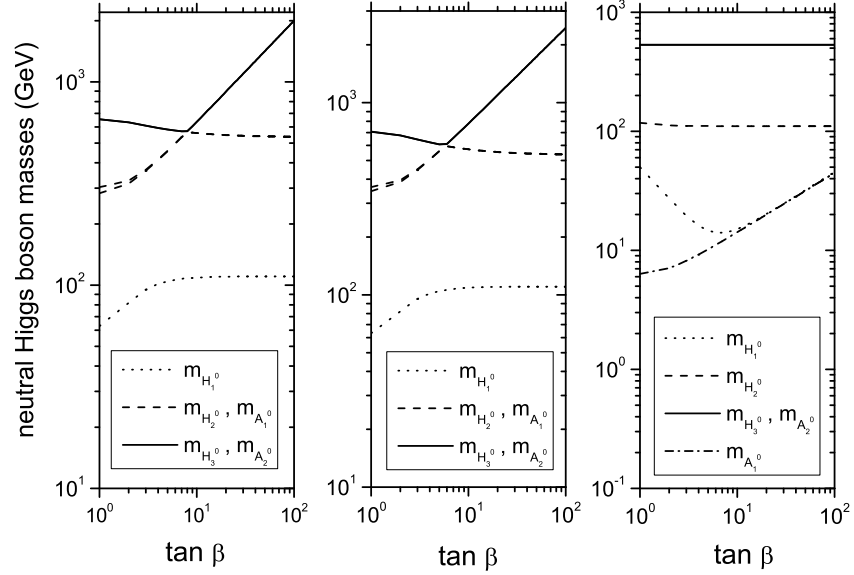


FIG. 10: Mass spectrum of the neutral Higgs bosons, taking $\mu_1 = 200$ GeV and $\lambda = 0.1$, for: $A = 200$ GeV (left), $A = 300$ GeV (center), $A = 0.1$ GeV (right).

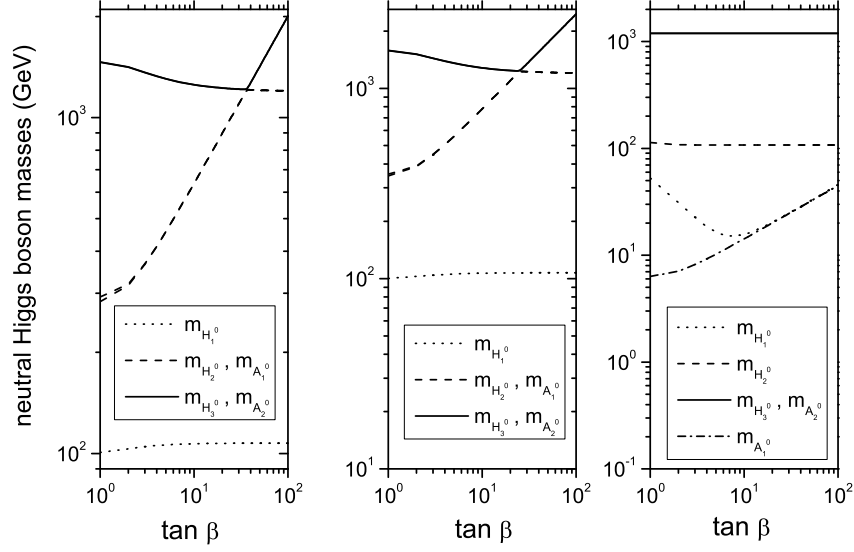


FIG. 11: Same as in Figure 10, but taking $\lambda = 0.5$.

The piece of Lagrangian containing the fermion couplings of the charged Higgs bosons is given by:

$$\mathcal{L}_{ffH_i^+} = -\frac{1}{\sqrt{2}v_D} \bar{u} \left[\left(\frac{m_d}{c_\beta} (\phi_1^-)^* - \frac{m_u}{s_\beta} \phi_2^+ \right) + \left(\frac{m_d}{c_\beta} (\phi_1^-)^* + \frac{m_u}{s_\beta} \phi_2^+ \right) \gamma_5 \right] d + h.c., \quad (18)$$

where $(\phi_1^-)^*$, ϕ_2^+ are related to the physical charged Higgs boson states (H_1^+, H_2^+, H_3^+) as follows:

$$\begin{aligned} (\phi_1^-)^* &= \sum_j^3 U_{2,j+1} H_j^+, \quad \phi_2^+ = \sum_j^3 U_{1,j+1} H_j^+, \\ H_j^+ &= (H_1^+, H_2^+, H_3^+). \end{aligned} \quad (19)$$

The U_{jk} 's denote the elements of the mixing-matrix that relates the physical charged Higgs bosons (H_1^+, H_2^+, H_3^+) and the Goldstone boson G^+ (which gives mass to the W^+) with the fields ϕ_2^+ , ϕ_1^{-*} , ξ_2^+ and ξ_1^{-*} as follows:

$$\begin{pmatrix} \phi_2^+ \\ \phi_1^{-*} \\ \xi_2^+ \\ \xi_1^{-*} \end{pmatrix} = \begin{pmatrix} U_{11} & U_{12} & U_{13} & U_{14} \\ U_{21} & U_{22} & U_{23} & U_{24} \\ U_{31} & U_{32} & U_{33} & U_{34} \\ U_{41} & U_{42} & U_{43} & U_{44} \end{pmatrix} \begin{pmatrix} G^+ \\ H_1^+ \\ H_2^+ \\ H_3^+ \end{pmatrix}. \quad (20)$$

Then, the couplings $\bar{u}dH_i^+$, $\bar{\nu}_l l H_i^+$ are given by:

$$\begin{aligned} g_{H_i^+ \bar{u}d} &= -\frac{i}{v_D \sqrt{2}} (A_i^{ud} + V_i^{ud} \gamma_5), \quad g_{H_i^- \bar{u}d} = -\frac{i}{v_D \sqrt{2}} (A_i^{ud} - V_i^{ud} \gamma_5), \\ g_{H_i^+ \bar{\nu}_l l} &= -\frac{i}{v_D \sqrt{2}} A_i^l (1 + \gamma_5), \quad g_{H_i^- \bar{\nu}_l l} = -\frac{i}{v_D \sqrt{2}} A_i^l (1 - \gamma_5), \end{aligned} \quad (21)$$

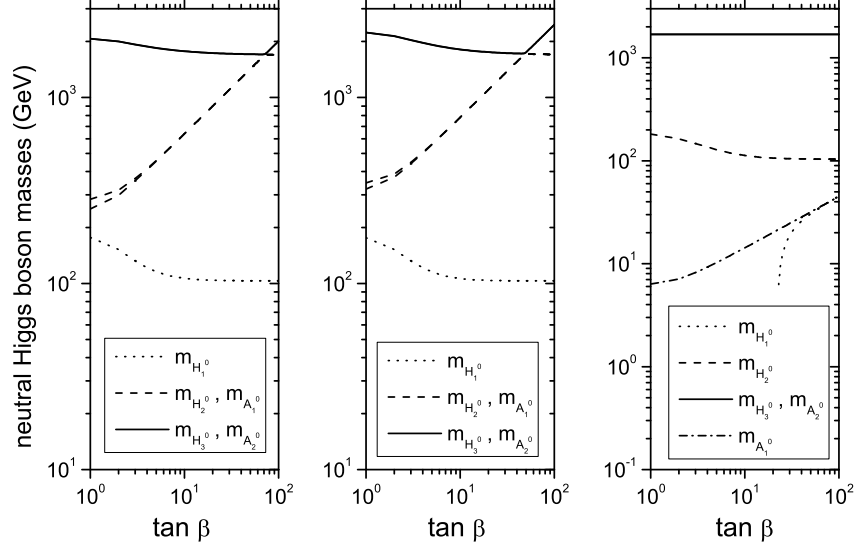


FIG. 12: Same as in Figure 10, but taking $\lambda = 1$.

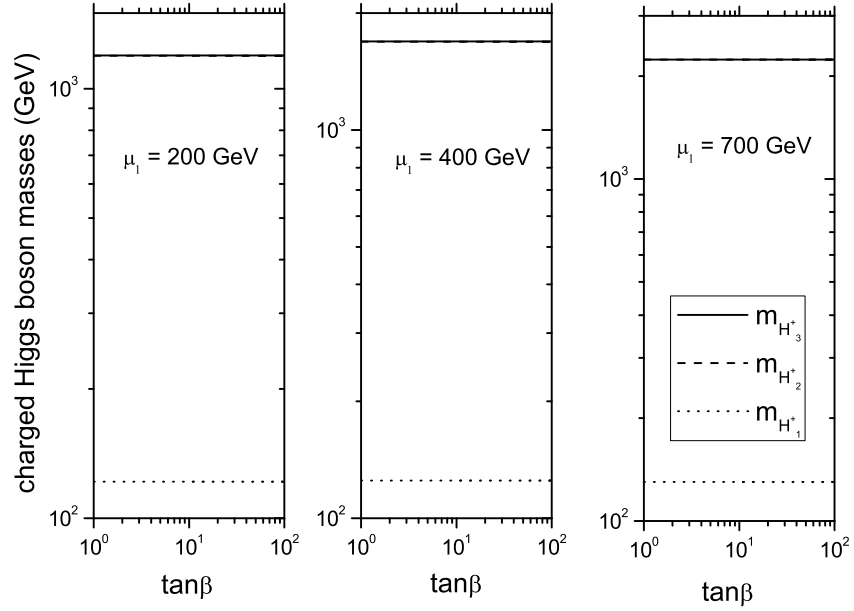


FIG. 13: Mass spectrum of the charged Higgs bosons, taking $A = 0$ GeV and $\lambda = 0.5$, for: $\mu_1 = 200$ GeV (left), $\mu_1 = 400$ GeV (center), $\mu_1 = 700$ GeV (right).

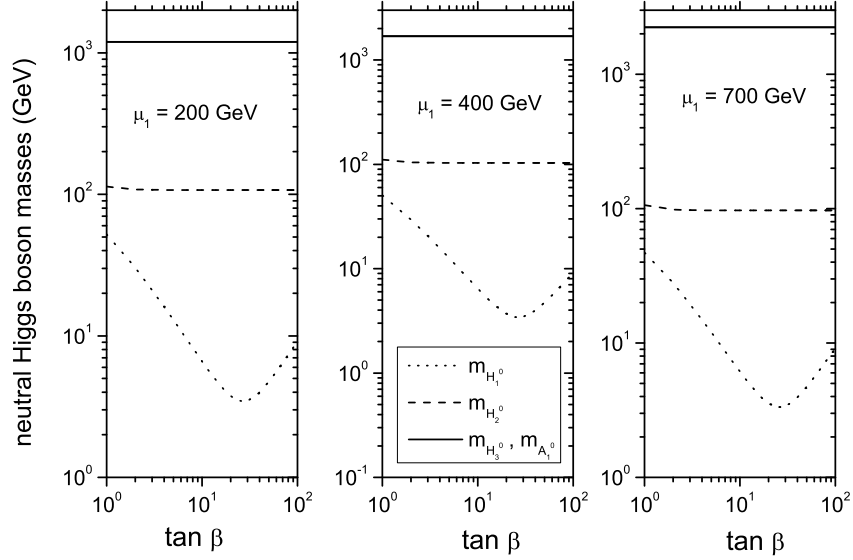


FIG. 14: Mass spectrum of the neutral Higgs bosons, taking $A = 0$ GeV and $\lambda = 0.5$, for: $\mu_1 = 200$ GeV (left), $\mu_1 = 400$ GeV (center), $\mu_1 = 700$ GeV (right). In this scenario (B) only one massive pseudoscalar appears, as one can see from the limit $A = 0$ (hence $B_1 = -A = 0$) an extra Goldstone boson should appear, as discussed in [10].

where A_i^{ud} and V_i^{ud} are defined as:

$$\begin{aligned}
 A_i^{ud} &= m_d t_\beta \frac{U_{2,i+1}}{s_\beta} - m_u \cot \beta \frac{U_{1,i+1}}{c_\beta}, \\
 V_i^{ud} &= m_d t_\beta \frac{U_{2,i+1}}{s_\beta} + m_u \cot \beta \frac{U_{1,i+1}}{c_\beta}, \\
 A_i^l &= m_l t_\beta \frac{U_{2,i+1}}{s_\beta}.
 \end{aligned} \tag{22}$$

One can see that the formulae in Eq. (10) become the couplings $\bar{u}dH_i^+$, $\bar{\nu}_l l H_i^+$ of the MSSM when we replace $U_{2,i+1} \rightarrow s_\beta$ and $U_{1,i+1} \rightarrow -c_\beta$ [2]. The vertex $\bar{u}dH_i^+$ induces at tree-level the decay $t \rightarrow H^+ b$, which will be studied in the next section.

B. The decay $t \rightarrow H_i^+ b$

In order to study this top quark BR we must consider both the decays $t \rightarrow H_i^+ b$ for $i = 1, 2$, because both modes could be kinematically allowed for several parameter configurations within

our model. The decay width of these modes takes the following form:

$$\begin{aligned} \Gamma(t \rightarrow H_i^+ b) &= \frac{g^2}{64\pi(m_W^2 - 2g^2 v_T^2)} m_t^3 \lambda^{1/2}(1, q_{H_i^+}, q_b) \\ &\times \left[(1 - q_{H_i^+} + q_b) \left(\frac{U_{1,i+1}^2}{s_\beta^2} + q_b \frac{U_{2,i+1}^2}{c_\beta^2} \right) - 4q_b \frac{U_{1,i+1} U_{2,i+1}}{s_\beta c_\beta} \right], \end{aligned} \quad (23)$$

where λ is the usual kinematic factor $\lambda(a, b, c) = (a - b - c)^2 - 4bc$ and $q_{b,H^+} = m_{b,H^+}^2/m_t^2$.

Furthermore, we shall neglect the decay width for the light fermion generations. As we mentioned before, if one replaces $U_{2,i+1} \rightarrow s_\beta$ and $U_{1,i+1} \rightarrow -c_\beta$, the formulae of the decay width also reduce to the MSSM case: see, e.g., [28]. In general the decay width for $t \rightarrow H_i^+ b$ depends on the Superpotential parameters through the elements $U_{(1,2),i+1}$. When we choose an MSSM+1CHT scenario where spontaneous EWSB is dominated by the effects of the Higgs doublets, the decay width is practically similar to the one obtained in the MSSM. If we do not, results can be very different in the two models. We shall discuss this in the forthcoming numerical analysis.

C. Numerical results for the decay $t \rightarrow H_i^+ b$ in the MSSM+1CHT

We explore several theoretically allowed regions of our MSSM+1CHT scenario and constrain these by using experimental bounds on the $\text{BR}(t \rightarrow H^+ b)$. In the so-called “tauonic Higgs model” [21], the decay mode ($H^+ \rightarrow \tau^+ \nu_\tau$) dominates the charged Higgs boson decay width, and $\text{BR}(t \rightarrow H^+ b)$ is constrained to be less than 0.4 at 95 % C.L. [21]. However, if no assumption is made on the charged Higgs boson decay, $\text{BR}(t \rightarrow H^+ b)$ is constrained to be less than 0.91 at 95 % C.L. [21]. Conversely, the combined LEP data excluded a charged Higgs boson with mass less than 79.3 GeV at 95 % C.L., a limit valid for an arbitrary $\text{BR}(H^+ \rightarrow \tau^+ \nu_\tau)$ [23, 29].

Thus, in order to conclude in this regard, we need to discuss all the charged Higgs boson decays following the steps of our previous paper [16]. In the present work, we shall evaluate all charged Higgs boson decays relevant masses below that of the top quark, thus including the modes $\tau^+ \nu_\tau, c\bar{s}, c\bar{b}, W^+ H_1^0, W^+ A_1^0$. In what follows, we want to find out whether a light charged Higgs boson (with $m_{H^\pm} \leq m_{W^\pm}$) is still allowed phenomenologically. As usual, we refer to our two benchmark scenarios.

Scenario A. Remember that this scenario was defined by taking $B_1 = \mu_1 = 0$, $B_2 = -A$, and $\mu_2 = 100$ GeV while for λ we considered the values $\lambda = 0.1, 0.5, 1.0$. In Figure 15 we present plots of: a) the $\text{BR}(t \rightarrow b H_1^+)$ vs. $\tan \beta$; b) the $\tan \beta - m_{H_1^+}$ plane; c) the $\text{BR}(t \rightarrow b H_2^+)$ vs. $\tan \beta$ and d) the $\tan \beta - m_{H_2^+}$ plane; for the case $\lambda = 0.1$, taking $A = 200, 300, 400$ GeV. We

can observe that both modes $t \rightarrow b H_i^+$ for $i = 1, 2$ are kinematically allowed. Also, we see that a charged Higgs boson with mass in the range $80 \text{ GeV} < m_{H_1^+} < 82 \text{ GeV}$ and for $1 < \tan \beta < 15$ satisfies the constraint $\text{BR}(t \rightarrow b H^+) < 0.4$. Furthermore, from the plots of Figure 16 we can see that in this scenario the dominant decay mode is into $\tau^+ \nu_\tau$, therefore they fall within the scope of the tauonic Higgs model, so that $\text{BR}(t \rightarrow H^+ b) \leq 0.4$ applies. This also happens for a heavier charged Higgs boson with mass in the range $125 \text{ GeV} < m_{H_2^+} < 160 \text{ GeV}$ and for $35 < \tan \beta < 100$. However, although this scenario is consistent with current experimental bounds from Tevatron on $\text{BR}(t \rightarrow b H^+)$, it is excluded after one considers the LEP2 limits on the neutral Higgs sector via $R_{H_1^0 Z^0 Z^0}$ [27].

In Figure 17 we present similar plots for the case $\lambda = 0.5$, taking $A = 200, 300, 400 \text{ GeV}$. We can observe that the mode $t \rightarrow b H_1^+$ satisfies the constraint $\text{BR}(t \rightarrow b H^+) < 0.4$ in the ranges $80 \text{ GeV} < m_{H_1^+} < 115 \text{ GeV}$ and $30 < \tan \beta < 100$. Then, from the plots of Figure 18, we see that in this range the dominant decay mode is into $\tau^+ \nu_\tau$, therefore they also fall within the realm of the tauonic Higgs model, so that $\text{BR}(t \rightarrow H^+ b) \leq 0.4$. Besides, this scenario is very interesting because we can have $m_{H^\pm} \sim m_{W^\pm}$ and a light neutral Higgs boson, which could be consistent with the experimental LEP2 limits, as discussed in section II and shown in Table I. In Figure 19 we present the corresponding plots for the case $\lambda = 1.0$, taking again $A = 200, 300, 400 \text{ GeV}$. We can observe that in this case only the mode $t \rightarrow b H_1^+$ is kinematically allowed and satisfies the constraint $\text{BR}(t \rightarrow b H^+) < 0.4$ in the ranges $140 \text{ GeV} < m_{H_1^+} < 160 \text{ GeV}$ and $60 < \tan \beta < 100$.

Scenario B. Recall that this was defined by taking $B_2 = \mu_2 = 0$, $B_1 = -A$, and $\mu_1 = 200 \text{ GeV}$ while for λ we considered the values $\lambda = 0.1, 0.5$. In Figure 20 we present plots of: a) the $\text{BR}(t \rightarrow b H_1^+)$ vs. $\tan \beta$; b) the $\tan \beta - m_{H_1^+}$ plane; for the case $\lambda = 0.1$, taking $A = 200, 300, 0.1 \text{ GeV}$. We can observe that the mode $t \rightarrow b H_1^+$ is kinematically allowed for the case $A = 0.1 \text{ GeV}$ and, if we combine the results of Table III, one can see that for charged Higgs boson masses in the range $84 \text{ GeV} < m_{H_1^+} < 89 \text{ GeV}$ and for $12 < \tan \beta < 50$ the model fulfills the constraint $\text{BR}(t \rightarrow b H^+) < 0.4$. Again we have a charged Higgs mass $\sim m_{W^\pm}$. Similarly, in Figure 21 we present similar plots but for the case $\lambda = 0.5$, taking $A = 200, 300, 0.1 \text{ GeV}$. We can observe here that the mode $t \rightarrow b H_1^+$ is kinematically permitted again for the case $A = 0.1$ and the model is fulfilling the constraint $\text{BR}(t \rightarrow b H^+) < 0.4$ in the ranges $121 \text{ GeV} < m_{H_1^+} < 129 \text{ GeV}$ and $20 < \tan \beta < 80$. In Figure 22 we present only a plot of the $\tan \beta - m_{H_1^+}$ plane, for the case $\lambda = 1.0$, taking $A = 200, 300, 0.1 \text{ GeV}$. We can deduce from here that the mode $t \rightarrow b H_1^+$ is kinematically

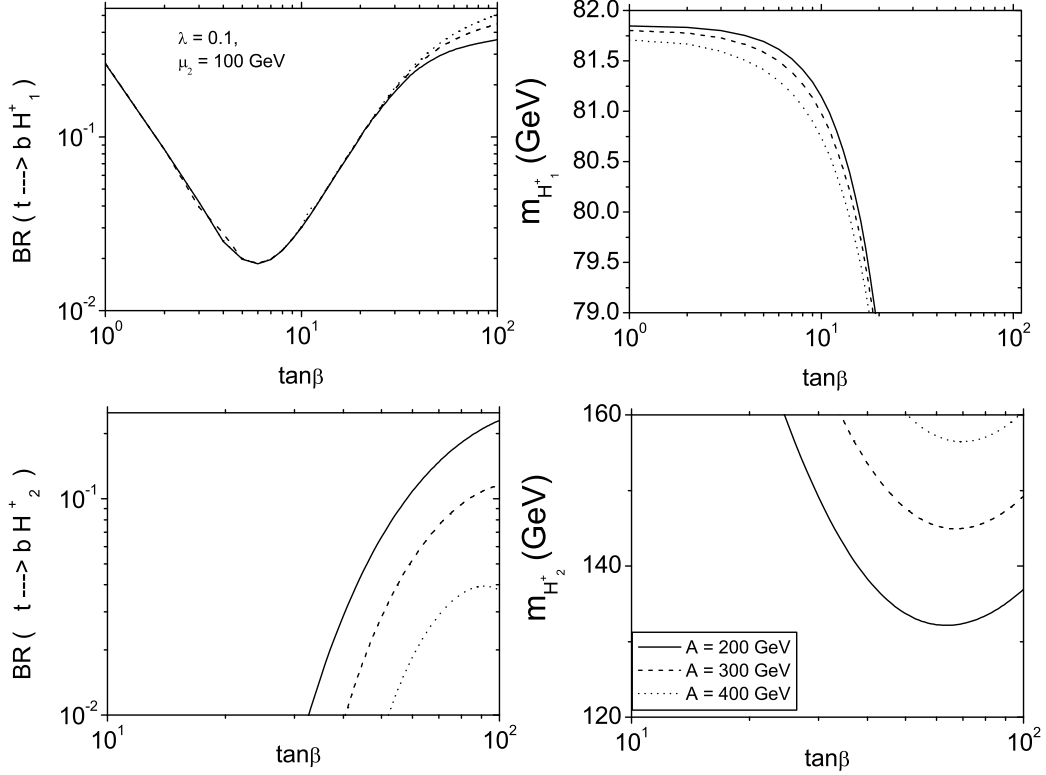


FIG. 15: It is plotted: a) the $\text{BR}(t \rightarrow b H_1^+)$ vs. $\tan \beta$ (top-left), b) the $\tan \beta - m_{H_1^+}$ plane (top-right), c) the $\text{BR}(t \rightarrow b H_2^+)$ vs. $\tan \beta$ (bottom-left), d) the $\tan \beta - m_{H_2^+}$ plane (bottom-right), in Scenario A by taking $\lambda = 0.1$, for: $A = 200$ GeV (solid), $A = 300$ GeV (dashes), $A = 400$ GeV (dots).

forbidden, because $m_{H_1^+} \approx 200$ GeV in the range $1 < \tan \beta < 100$. Finally, in Figure 23 we present plots of: a) the $\text{BR}(t \rightarrow b H_1^+)$ vs. $\tan \beta$; b) the $\tan \beta - m_{H_1^+}$ plane, for the case $\lambda = 0.5$ and $A = 0$, taking $\mu_1 = 200, 400, 700$ GeV. We note here that the mode $t \rightarrow b H_1^+$ is kinematically allowed and we see that a charged Higgs boson with mass in the range $121 \text{ GeV} < m_{H_1^+} < 131 \text{ GeV}$ and for $1 < \tan \beta < 70$ satisfies the constraint $\text{BR}(t \rightarrow b H^+) < 0.4$. Combining the results of Table IV, one can observe that only the small region $1 < \tan \beta < 6$ is allowed by the LEP collaborations' results.

D. Decays of charged Higgs bosons in the MSSM+1CHT

Let us now discuss the decay modes of the charged Higgs bosons within our model, which have an interest independently of whether these states are themselves produced in top decays. As usual,

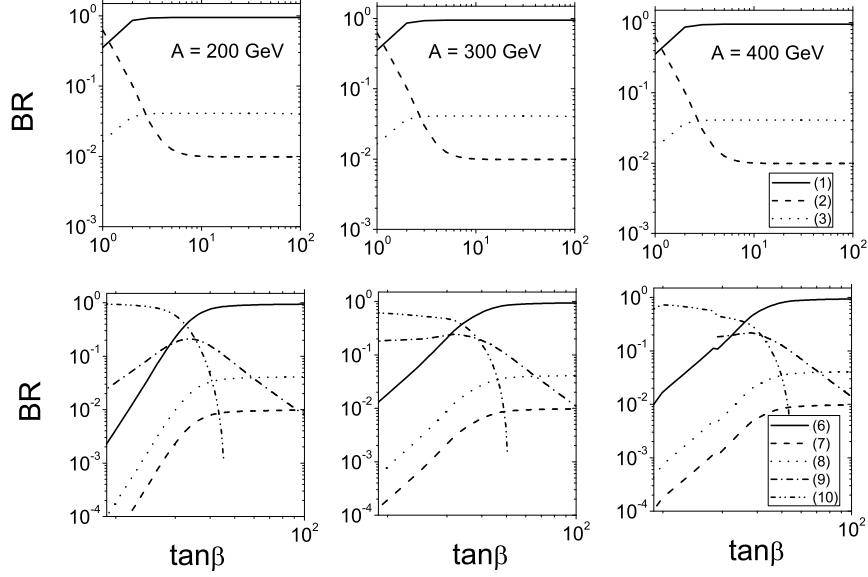


FIG. 16: The figure shows the branching ratios of H_1^+ (top) and H_2^+ (bottom) decaying into the principal modes in Scenario A, with $\lambda = 0.1$ and $\mu_2 = 100$ GeV, for: $A = 200$ GeV (left), $A = 300$ GeV (center), $A = 400$ GeV (right). The lines correspond to: (1) $\text{BR}(H_1^+ \rightarrow \tau^+ \nu_\tau)$, (2) $\text{BR}(H_1^+ \rightarrow c\bar{s})$, (3) $\text{BR}(H_1^+ \rightarrow c\bar{b})$, (6) $\text{BR}(H_2^+ \rightarrow \tau^+ \nu_\tau)$, (7) $\text{BR}(H_2^+ \rightarrow c\bar{s})$, (8) $\text{BR}(H_2^+ \rightarrow c\bar{b})$, (9) $\text{BR}(H_2^+ \rightarrow W^+ H_1^0)$, (10) $\text{BR}(H_2^+ \rightarrow W^+ A_1^0)$.

we refer to our two customary benchmark scenarios.

Scenario A. In Figure 16 we present the BR's of the channels $H_i^+ \rightarrow \tau^+ \nu_\tau, c\bar{s}, c\bar{b}, W^+ H_1^0, W^+ A_1^0$ for $i = 1, 2$ as a function of $\tan \beta$ in the range $1 < \tan \beta < 100$ for the case $\lambda = 0.1$, taking $A = 200, 300, 400$ GeV. When $t \rightarrow bH_i^+$ is kinematically allowed for both $i = 1, 2$, the dominant decay of the charged Higgs bosons is via the mode $\tau^+ \nu_\tau$, with $\text{BR}(H_i^+ \rightarrow \tau^+ \nu_\tau) \approx 1$. We can observe that for H_2^+ the decay mode $W^+ A_1^0$ is dominant for $\tan \beta < 30$, although the decay $t \rightarrow bH_2^+$ is not kinematically allowed. In Figure 18 we present similar plots for H_1^+ , but now with $\lambda = 0.5$ and again in this case the dominant decay mode is into $\tau^+ \nu_\tau$ for the range $\tan \beta > 15$. Then, from Figure 18 one gets that $\text{BR}(H_i^+ \rightarrow \tau^+ \nu_\tau) \approx 1$ when $t \rightarrow bH_1^+$ is kinematically allowed. Similarly, in Figure 24 we present the corresponding plots for H_1^+ in the case $\lambda = 1.0$. For $A = 200$ GeV the dominant decay of the considered charged Higgs boson is the mode $\tau^+ \nu_\tau$, except in the range $15 < \tan \beta < 35$, where the decay channel $W^+ H_1^0$ is also relevant. For $A = 300, 400$ GeV the dominant decay of the charged Higgs state is via the mode $\tau^+ \nu_\tau$ when $\tan \beta > 35$, but for $12 < \tan \beta < 35$ the decay channel $W^+ H_1^0$ becomes the leading one whereas for the range

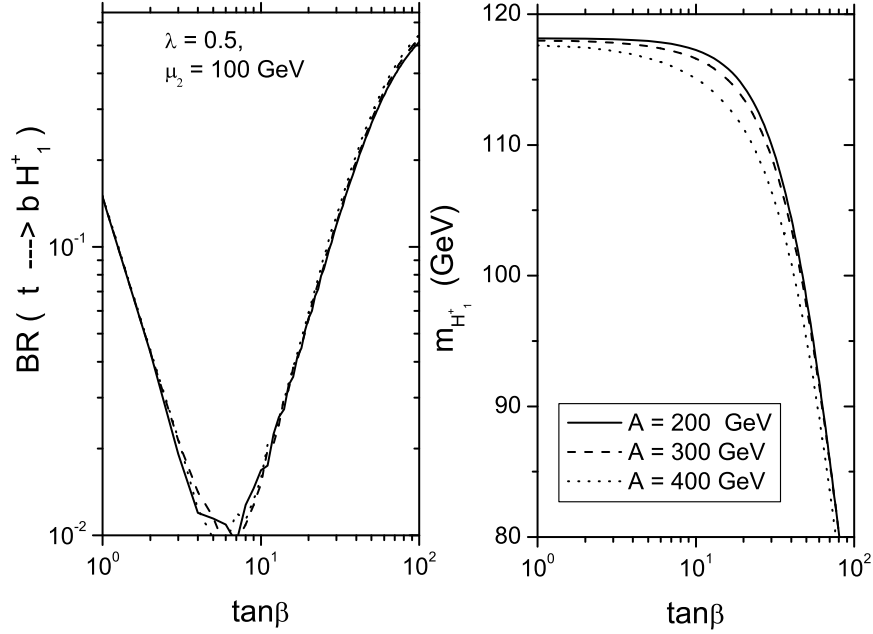


FIG. 17: It is plotted: the $\text{BR}(t \rightarrow b H_1^+)$ vs. $\tan \beta$ (left), the $\tan \beta - m_{H_1^+}$ plane (right), in Scenario A taking $\lambda = 0.5$, for: $A = 200$ GeV (solid), $A = 300$ GeV (dashes), $A = 400$ GeV (dots).

$2 < \tan \beta < 9$ the mode $W^+ A_1^0$ is dominant.

Now we discuss the decay modes of H_3^+ for the case $\lambda = 0.1$. We can see in Figure 25 for $A = 200$ GeV that the mode $t\bar{b}$ is dominant when $\tan \beta < 2$, but for $2 < \tan \beta$ the mode $W^+ A_1^0$ is the leading one. For the case $A = 300$ GeV there are three dominant decay modes: $W^+ H_2^0$ in the range $\tan \beta < 2$, $W^+ H_1^0$ for $2 < \tan \beta < 60$ and $t\bar{b}$ when $60 < \tan \beta$. For $A = 400$ GeV the relevant decay channels are: $W^+ H_2^0$ in the range $\tan \beta < 2$, $W^+ H_1^0$ for the two ranges $2 < \tan \beta < 10$ and $20 < \tan \beta < 40$, $W^+ A_1^0$ for $10 < \tan \beta < 20$, $t\bar{b}$ when $40 < \tan \beta$. In Figure 26 we present the corresponding plots for the BR's of the channels $H_i^+ \rightarrow \tau^+ \nu_\tau, t\bar{b}, W^+ H_j^0, W^+ A_1^0, W^+ Z^0$ for $i = 2, 3, j = 1, 2$ as a function of $\tan \beta$ in the range $1 < \tan \beta < 100$ for the case $\lambda = 0.5$, taking $A = 200, 300, 400$ GeV. When $A = 200$ GeV the dominant decay modes for H_2^+ are: $W^+ A_1^0$ in the range $\tan \beta < 25$ and $t\bar{b}$ for $25 < \tan \beta$. We obtain similar results for H_3^+ , except for $\tan \beta < 2$, where the mode $W^+ H_1^0$ is dominant. For the cases $A = 300, 400$ GeV the relevant decay modes of H_2^+ are: $W^+ Z^0$ when $\tan \beta < 4$, $W^+ A_1^0$ in the range $4 < \tan \beta < 25$ and $t\bar{b}$ for $25 < \tan \beta$. As for H_2^+ , we obtain the same dominant modes as for H_3^+ in the range $4 < \tan \beta$, because the decay channel $W^+ H_1^0$ is relevant for $\tan \beta < 4$. In Figure 27 we present plots for the BR's of the channels $H_i^+ \rightarrow \tau^+ \nu_\tau, t\bar{b}, W^+ H_j^0, W^+ A_1^0, W^+ Z^0$ for $i = 2, 3, j = 1, 2$ as a function of $\tan \beta$ in the

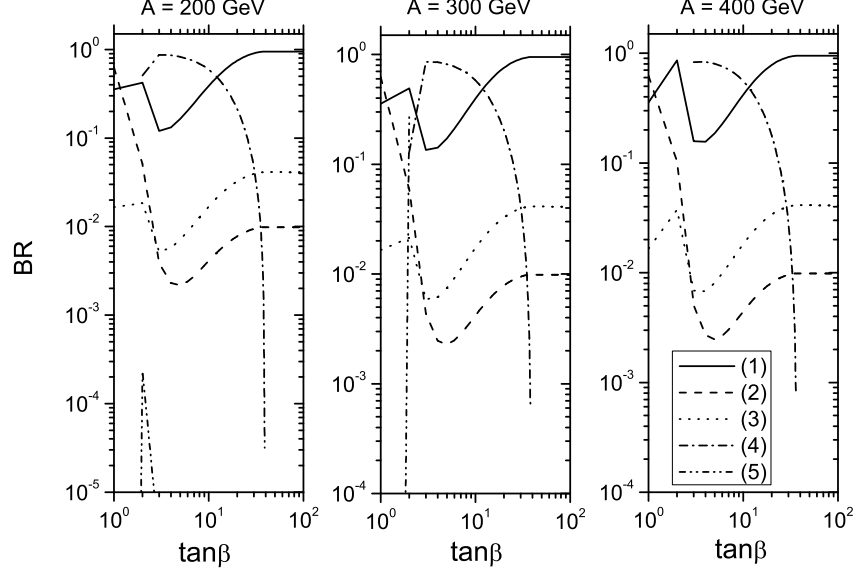


FIG. 18: The figure shows the branching ratios of H_1^+ decaying into the principal modes in Scenario A, with $\lambda = 0.5$ and $\mu_2 = 100$ GeV, for: $A = 200$ GeV (left), $A = 300$ GeV (center), $A = 400$ GeV (right). The lines correspond to: (1) $\text{BR}(H_1^+ \rightarrow \tau^+ \nu_\tau)$, (2) $\text{BR}(H_1^+ \rightarrow c\bar{s})$, (3) $\text{BR}(H_1^+ \rightarrow c\bar{b})$, (4) $\text{BR}(H_1^+ \rightarrow W^+ H_1^0)$, (5) $\text{BR}(H_1^+ \rightarrow W^+ A_1^0)$.

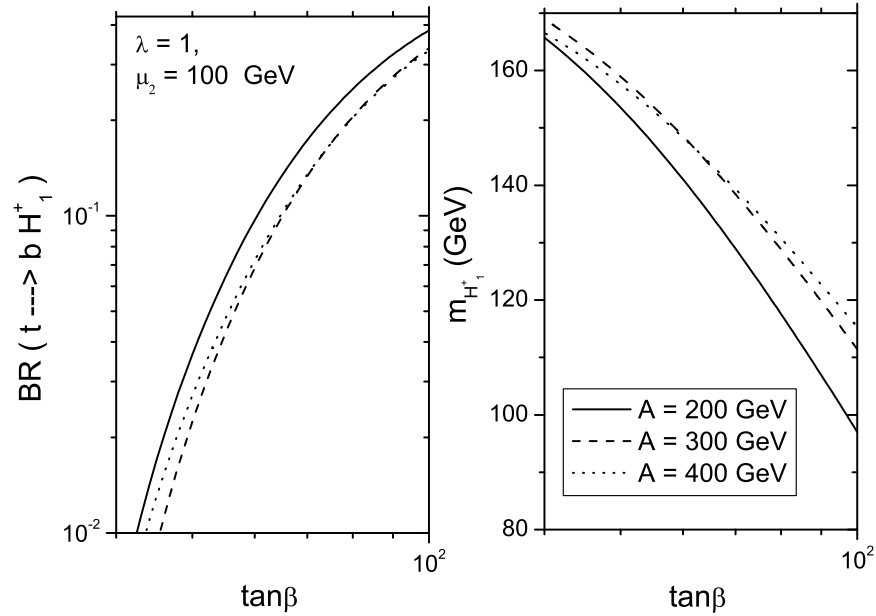


FIG. 19: Same as Figure 17, but taking $\lambda = 1$.

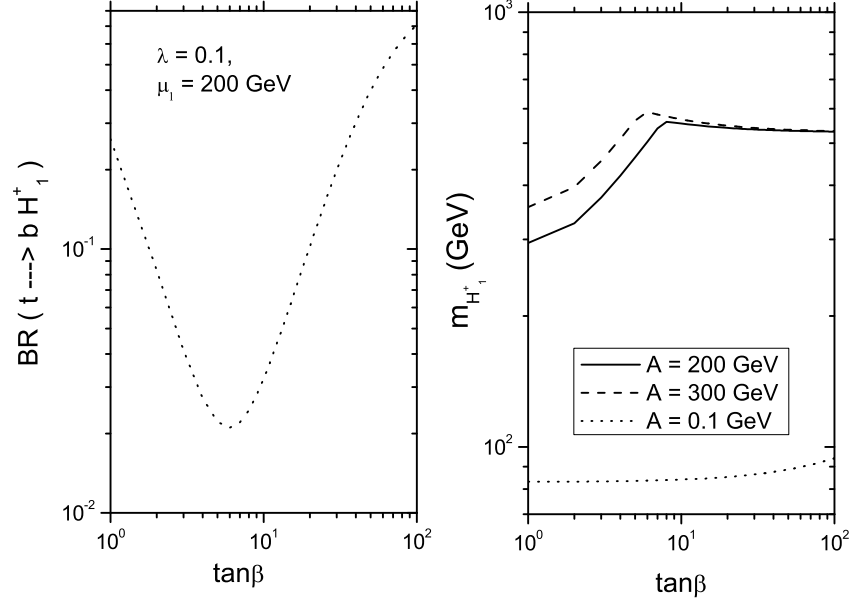


FIG. 20: It is plotted: $\text{BR}(t \rightarrow b H_1^+)$ vs. $\tan \beta$ (left), the $\tan \beta - m_{H_1^+}$ plane (right), in Scenario B, taking $\lambda = 0.1$ for: $A = 200$ GeV (solid), $A = 300$ GeV (dashes), $A = 0.1$ GeV (dots).

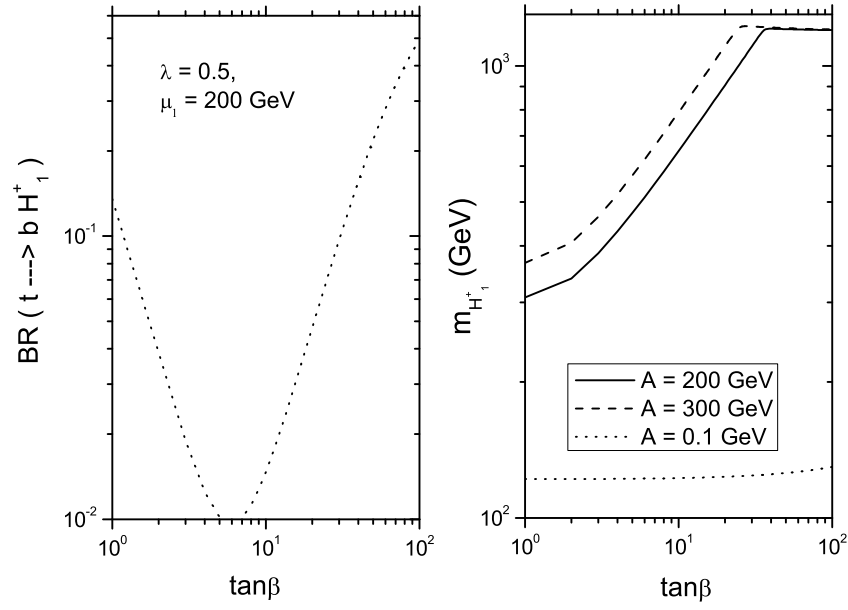


FIG. 21: Same as Figure 20, but taking $\lambda = 0.5$.

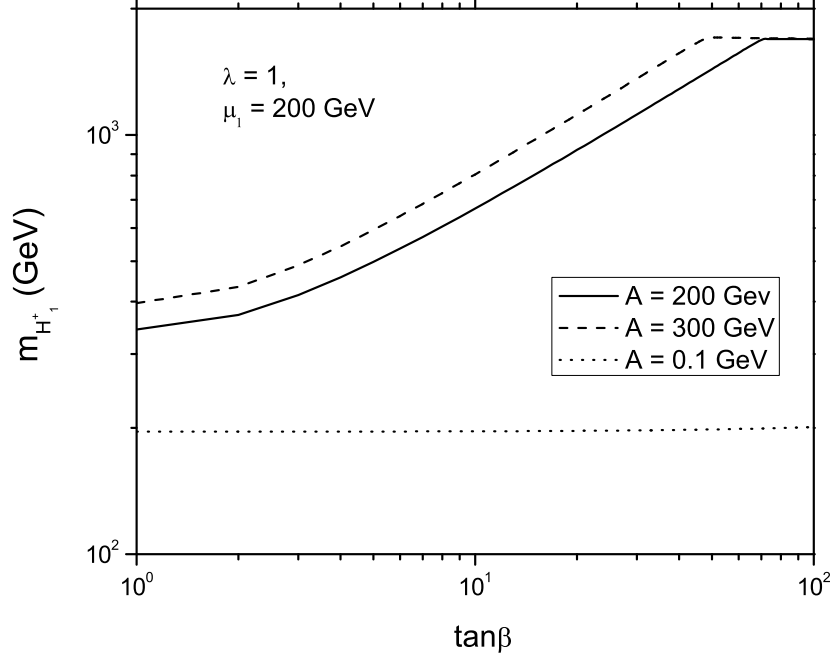


FIG. 22: The $\tan\beta - m_{H_1^+}$ plane, in Scenario B, taking $\lambda = 1.0$ for: $A = 200$ GeV (solid), $A = 300$ GeV (dashes), $A = 0.1$ GeV (dots).

range $1 < \tan\beta < 100$ for the case $\lambda = 1$, taking $A = 200, 300, 400$ GeV. As in the case $\lambda = 0.5$, when $A = 200$ GeV the dominant decay modes for H_2^+ are: $W^+A_1^0$ in the range $\tan\beta < 25$, $t\bar{b}$ for $25 < \tan\beta$. We obtain similar results for H_3^+ , except for $\tan\beta < 2$ where the mode $t\bar{b}$ is dominant. For the cases $A = 300, 400$ GeV the relevant decay modes of H_2^+ are: W^+Z^0 when $\tan\beta < 4$, $W^+A_1^0$ in the range $4 < \tan\beta < 25$ and $t\bar{b}$ for $25 < \tan\beta$. We get the following dominant modes for H_3^+ : $W^+H_2^0$ for $1.5 < \tan\beta < 2$, $W^+A_1^0$ when $2 < \tan\beta < 25$ while in two ranges $\tan\beta < 1.5$ and $25 < \tan\beta$ the mode $t\bar{b}$ becomes the most important one.

Scenario B. In Figure 28 we present the $\text{BR}(H_i^+ \rightarrow \tau^+\nu_\tau, c\bar{s}, c\bar{b}, W^+H_1^0, W^+A_1^0)$'s as a function of $\tan\beta$ in the range $1 < \tan\beta < 100$ for the case $A = 0.1$ GeV, taking $\lambda = 0.1, 0.5$. When the mode $t \rightarrow bH_1^+$ is kinematically allowed, the dominant decay of the charged Higgs bosons is via the mode $\tau^+\nu_\tau$ and it is obtained that $\text{BR}(H_1^+ \rightarrow \tau^+\nu_\tau) \approx 1$. We can observe that for $\lambda = 0.5$ the mode $W^+A_1^0$ is dominant for $2 < \tan\beta < 15$. In Figure 29 we present $\text{BR}(H_i^+ \rightarrow \tau^+\nu_\tau, c\bar{s}, c\bar{b}, W^+H_1^0, W^+A_1^0)$'s as a function of $\tan\beta$ in the range $1 < \tan\beta < 100$ for the case $A = 0$ GeV, $\lambda = 0.5$, taking $\mu_1 = 200, 400, 700$ GeV. In these cases the decay $t \rightarrow bH_1^+$ is kinematically

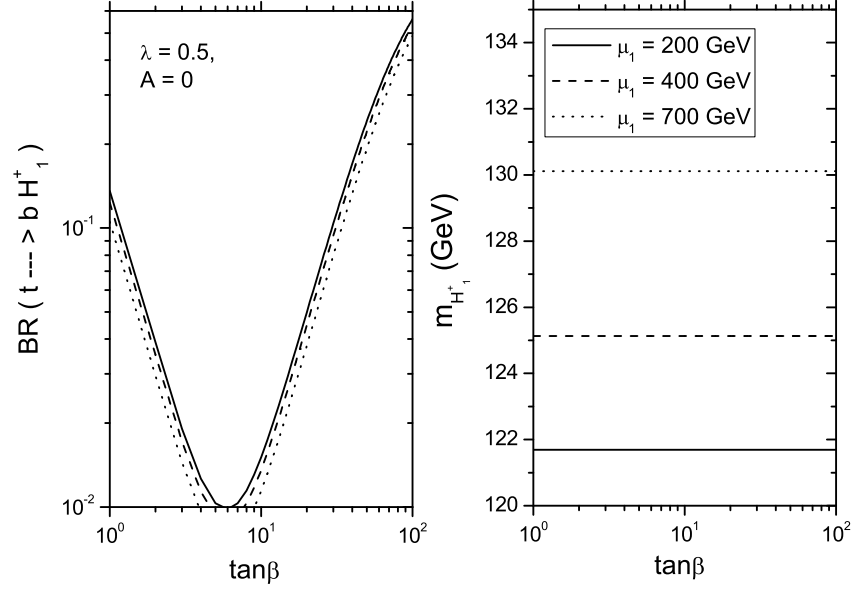


FIG. 23: It is plotted: $BR(t \rightarrow b H_1^+)$ vs. $\tan\beta$ (left), the $\tan\beta - m_{H_1^+}$ plane (right), in Scenario B, taking $\lambda = 0.5$ and $A = 0$ for: $\mu_1 = 200$ GeV (solid), $\mu_1 = 400$ GeV (dashes), $\mu_1 = 700$ (dots).

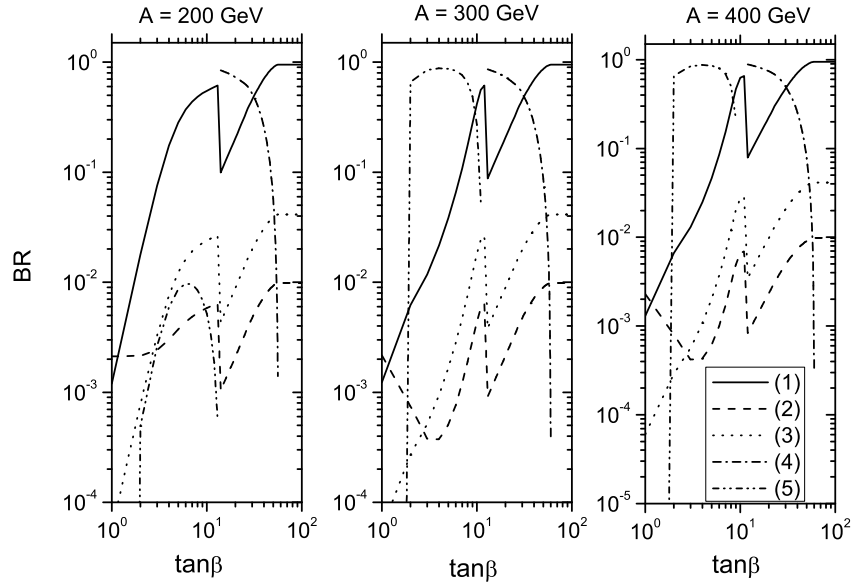


FIG. 24: Same as Figure 18 but taking $\lambda = 1$.

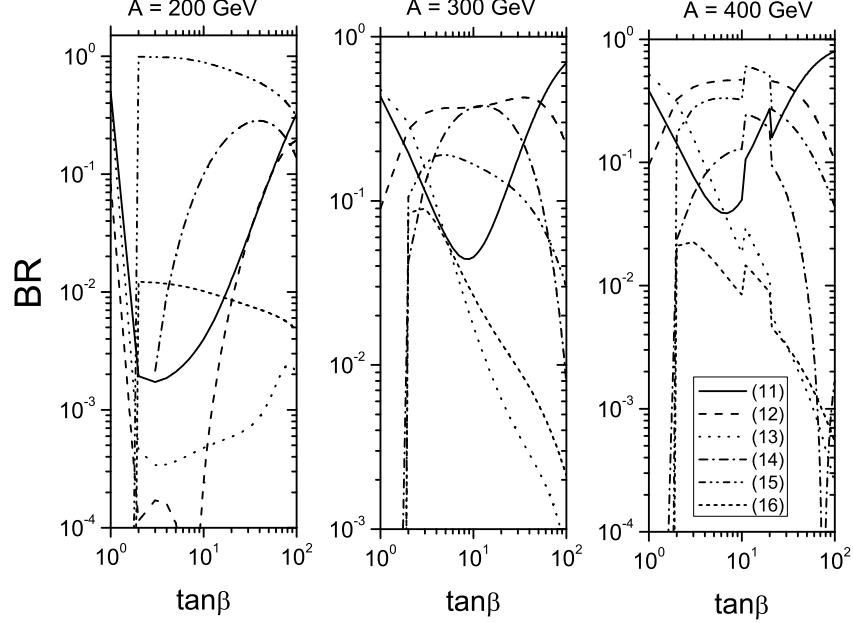


FIG. 25: The figure shows the branching ratios of H_3^+ decaying into the principal modes in Scenario A, taking $\lambda = 0.1$ and $\mu_2 = 100$ GeV for: $A = 200$ GeV (left), $A = 300$ GeV (center), $A = 400$ GeV (right). The lines correspond to: (11) $\text{BR}(H_3^+ \rightarrow t\bar{b})$, (12) $\text{BR}(H_3^+ \rightarrow W^+ H_1^0)$, (13) $\text{BR}(H_3^+ \rightarrow W^+ H_2^0)$, (14) $\text{BR}(H_3^+ \rightarrow W^+ H_3^0)$, (15) $\text{BR}(H_3^+ \rightarrow W^+ A_1^0)$, (16) $\text{BR}(H_3^+ \rightarrow W^+ Z^0)$.

allowed and the dominant decay of the charged Higgs boson is via $\tau^+ \nu_\tau$ for $\tan \beta > 20$, since $\text{BR}(H_1^+ \rightarrow \tau^+ \nu_\tau) \approx 1$. In contrast, when $\tan \beta < 20$ the mode $W^+ H_1^0$ is dominant.

In Figure 30 we present the BR's of the relevant decay channels of the charged Higgs H_1^+ for $A = 200, 300$ GeV, taking $\lambda = 0.1$. When $\tan \beta < 6$ the dominant mode is $t\bar{b}$. When $6 < \tan \beta$ though, the dominant mode becomes $W^+ Z^0$. In Figure 31 we observe that for the same previous values for A , but with $\lambda = 0.5$, the dominant decays channels are: $t\bar{b}$ for $\tan \beta < 40$ and $W^+ Z^0$ for $\tan \beta > 40$.

In Figure 32 we present plots for the BR's of the channels $H_i^+ \rightarrow t\bar{b}, W^+ H_j^0, W^+ A_1^0, W^+ Z^0$ for $i = 2, 3, j = 1, 2$ as a function of $\tan \beta$ in the range $1 < \tan \beta < 100$ for the case $\lambda = 0.1$, taking $A = 0.1, 200, 300$ GeV. When $A = 0.1$ GeV the dominant decay modes for H_2^+ are: $t\bar{b}$ for $\tan \beta < 2$ and $W^+ Z^0$ when $2 < \tan \beta$. For H_3^+ the mode $W^+ Z^0$ is the dominant one in the range $1 < \tan \beta < 100$. For $A = 200, 300$ GeV the relevant decay modes of H_2^+ are: $t\bar{b}$ when $\tan \beta < 2$ and $W^+ Z^0$ when $2 < \tan \beta$. We obtain similar results for H_3^+ , but now the mode $W^+ Z^0$ is dominant when $6 < \tan \beta$, and $t\bar{b}$ is the relevant mode for $\tan \beta < 6$. In Figure 33 we present plots for the

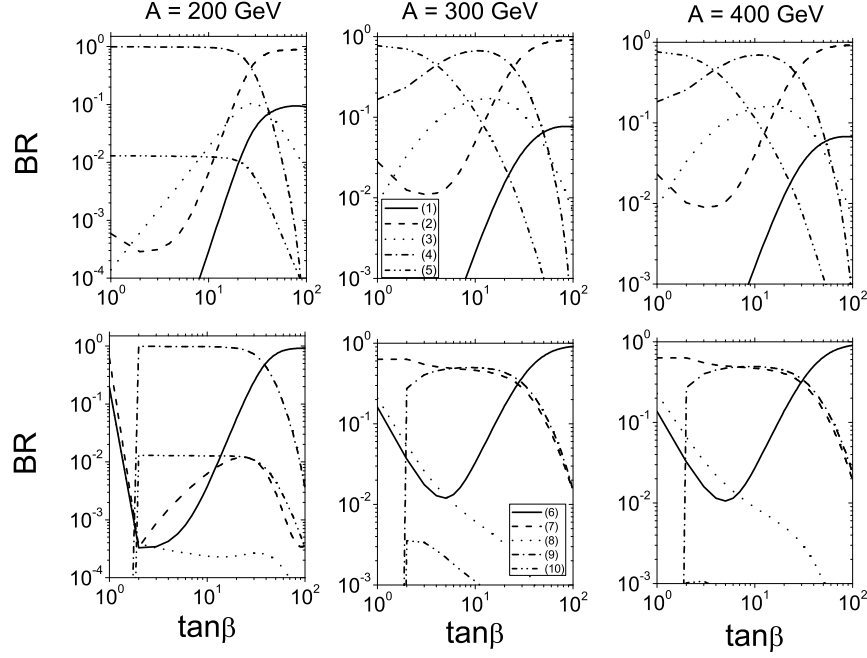


FIG. 26: The figure shows the branching ratios of H_2^+ (top) and H_3^+ (bottom) decaying into the principal modes in Scenario A, taking $\lambda = 0.5$ and $\mu_2 = 100$ GeV for $A = 200$ GeV (left), $A = 300$ GeV (center), $A = 400$ GeV (right). The lines correspond to: (1) $\text{BR}(H_2^+ \rightarrow \tau^+ \nu_\tau)$, (2) $\text{BR}(H_2^+ \rightarrow t\bar{b})$, (3) $\text{BR}(H_2^+ \rightarrow W^+ H_1^0)$, (4) $\text{BR}(H_2^+ \rightarrow W^+ A_1^0)$, (5) $\text{BR}(H_2^+ \rightarrow W^+ Z^0)$, (6) $\text{BR}(H_3^+ \rightarrow t\bar{b})$, (7) $\text{BR}(H_3^+ \rightarrow W^+ H_1^0)$, (8) $\text{BR}(H_3^+ \rightarrow W^+ H_2^0)$, (9) $\text{BR}(H_3^+ \rightarrow W^+ A_1^0)$, (10) $\text{BR}(H_3^+ \rightarrow W^+ Z^0)$.

BR's of channels $H_i^+ \rightarrow t\bar{b}, W^+ H_j^0, W^+ A_1^0, W^+ Z^0$ for $i = 2, 3, j = 1, 2$ as a function of $\tan \beta$ in the range $1 < \tan \beta < 100$, taking $\lambda = 0.5$ for $A = 0.1, 200, 300$ GeV. When $A = 0.1$ GeV the dominant decay modes for H_2^+ become: $W^+ H_1^0$ in the range $\tan \beta < 1.5$, $t\bar{b}$ for $1.5 < \tan \beta$ and $W^+ Z^0$ when $2 < \tan \beta$. For H_3^+ the mode $W^+ Z^0$ is dominant for all $\tan \beta$. For $A = 200, 300$ GeV the relevant decay modes of H_2^+ are: $W^+ H_2^0$ when $2 < \tan \beta$ and $W^+ Z^0$ for $2 < \tan \beta$. Similar dominant modes are obtained for H_3^+ , but now when $\tan \beta < 30$ the mode $W^+ Z^0$ becomes the principal one, and for $30 < \tan \beta$ the mode $t\bar{b}$ is the relevant one. In Figure 34 we present plots for the BR's of the channels $H_1^+ \rightarrow \tau^+ \nu_\tau, t\bar{b}, W^+ H_1^0, W^+ A_1^0, W^+ Z^0$ as a function of $\tan \beta$ in the range $1 < \tan \beta < 100$ for $\lambda = 1$, taking $A = 0.1, 200, 300$ GeV. For $A = 0.1$ GeV the dominant decay modes for H_1^+ are: $W^+ A_1^0$ in the range $2 < \tan \beta < 40$, $t\bar{b}$ for $\tan \beta < 2$ and $40 < \tan \beta$. For $A = 200$ (300) GeV the relevant decay modes of H_2^+ are: $t\bar{b}$ when $\tan \beta < 70$ (50) and $W^+ A_1^0$ when 70 (50) $< \tan \beta$. In Figure 35 we present plots for the BR's of channels $H_i^+ \rightarrow t\bar{b}, W^+ H_j^0, W^+ A_1^0, W^+ Z^0$ for $i = 2, 3, j = 1, 2$ as a function of $\tan \beta$ in the range $1 < \tan \beta < 100$, taking $\lambda = 1$ for $A = 0.1, 200, 300$ GeV.

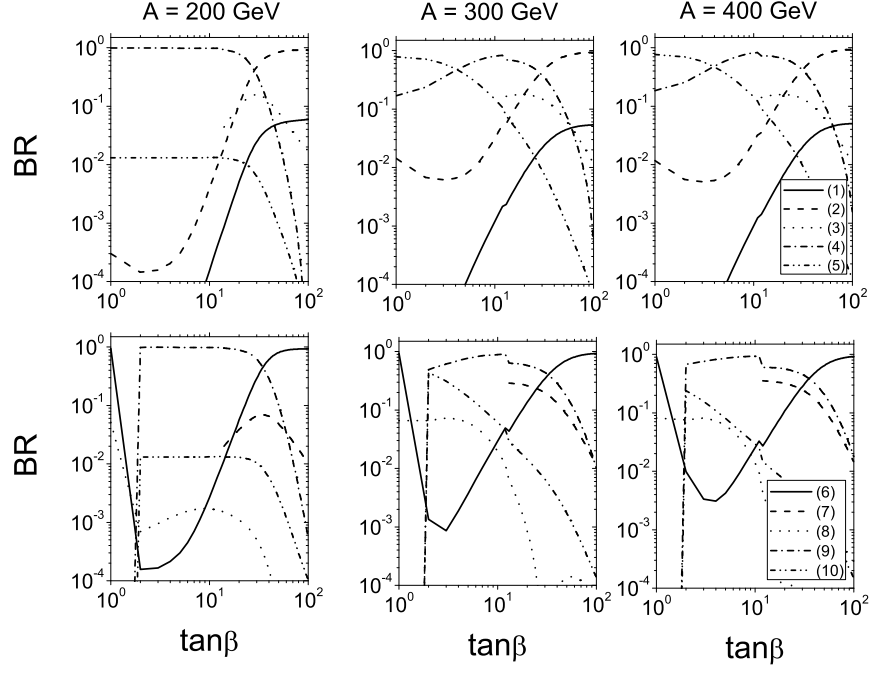


FIG. 27: Same as Figure 26, but taking $\lambda = 1$.

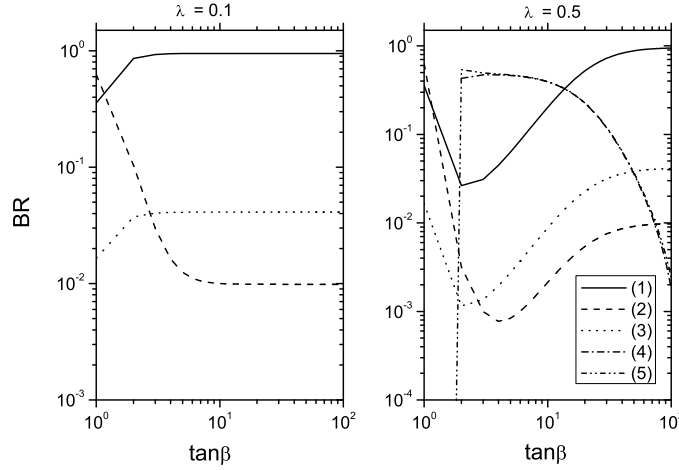


FIG. 28: The figure shows the branching ratios of H_1^+ decaying into the principal modes in Scenario B considering the cases: $\lambda = 0.1$ (left), $\lambda = 0.5$ (right), with $A = 0.1$ GeV and $\mu_1 = 200$ GeV. The lines correspond to: (1) $\text{BR}(H_1^+ \rightarrow \tau^+ \nu_\tau)$, (2) $\text{BR}(H_1^+ \rightarrow c \bar{s})$, (3) $\text{BR}(H_1^+ \rightarrow c \bar{b})$, (4) $\text{BR}(H_1^+ \rightarrow W^+ H_1^0)$, (5) $\text{BR}(H_1^+ \rightarrow W^+ A_1^0)$.

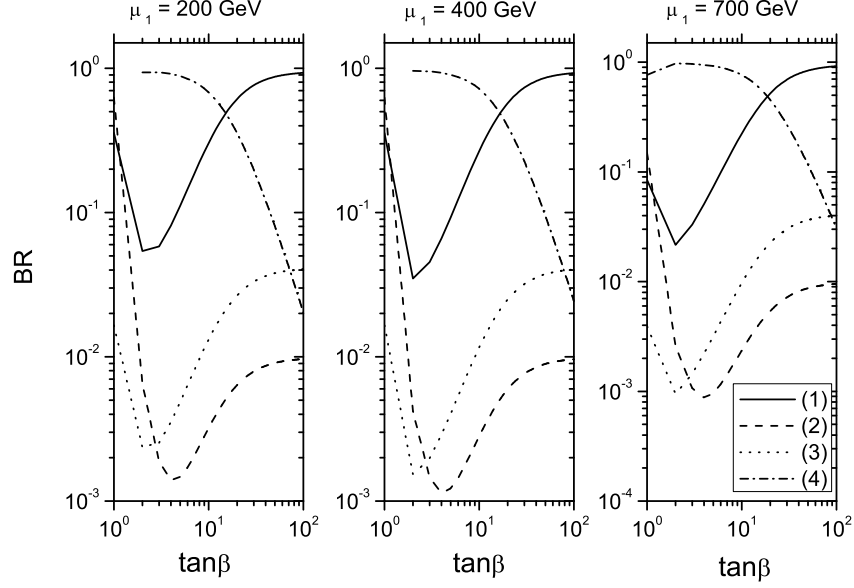


FIG. 29: The figure shows the branching ratios of H_1^+ decaying into the principal modes in Scenario B, with $\lambda = 0.5$ and $A = 0$ GeV for: $\mu_1 = 200$ GeV (left), $\mu_1 = 400$ GeV (center), $\mu_1 = 700$ GeV (right). The lines correspond to: (1) $\text{BR}(H_1^+ \rightarrow \tau^+ \nu_\tau)$, (2) $\text{BR}(H_1^+ \rightarrow c\bar{s})$, (3) $\text{BR}(H_1^+ \rightarrow c\bar{b})$, (4) $\text{BR}(H_1^+ \rightarrow W^+ H_1^0)$.

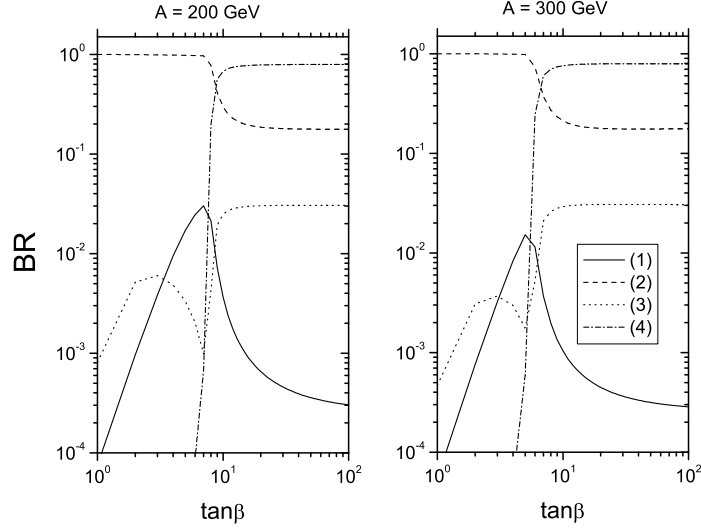


FIG. 30: The figure shows the branching ratios of H_1^+ decaying into the principal modes in Scenario B taking $\lambda = 0.1$ GeV and $\mu_1 = 200$ GeV, for: $A = 200$ GeV (left), $A = 300$ GeV (right). The lines correspond to: (1) $\text{BR}(H_1^+ \rightarrow \tau^+ \nu_\tau)$, (2) $\text{BR}(H_1^+ \rightarrow t\bar{b})$, (3) $\text{BR}(H_1^+ \rightarrow W^+ H_1^0)$, (4) $\text{BR}(H_1^+ \rightarrow W^+ Z^0)$.

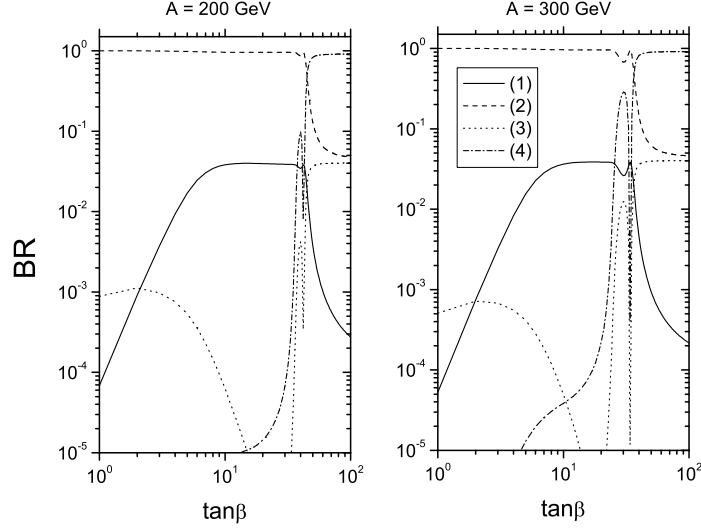


FIG. 31: Same as Figure 30, but taking $\lambda = 0.5$.

As in the case $\lambda = 0.5$, when $A = 0.1$ GeV the dominant decay modes for H_2^+ are: $t\bar{b}$ for $\tan\beta < 2$ and W^+Z^0 when $2 < \tan\beta$. For H_3^+ the mode W^+Z^0 is dominant for the entire $\tan\beta$ range. For the case $A = 200$ (300) GeV the relevant decay modes of H_2^+ are: $W^+H_2^0$ when $2 < \tan\beta$, W^+Z^0 for $2 < \tan\beta < 60(50)$, $t\bar{b}$ when $60(50) < \tan\beta < 100(70)$. The dominant modes for the H_3^+ are: W^+Z^0 in the range $\tan\beta < 60$, and for $60 < \tan\beta$ the mode $t\bar{b}$ is relevant. In Figure 36 we present the corresponding plots for the BR's of the channels $H_i^+ \rightarrow t\bar{b}, W^+H_j^0, W^+A_1^0, W^+Z^0$ for $i = 2, 3$, $j = 1, 2$ as a function of $\tan\beta$ in the range $1 < \tan\beta < 100$, taking $\lambda = 0.5$ for $\mu_1 = 200, 400, 700$ GeV with $A = 0$ GeV. The dominant decay modes for H_2^+ are: $W^+H_2^0$ in the range $\tan\beta < 1.5$, $t\bar{b}$ for $1.5 < \tan\beta < 2$ and W^+Z^0 when $2 < \tan\beta$. For H_3^+ the mode W^+Z^0 is dominant for all values of $\tan\beta$. For the case $\mu_1 = 400, 700$ GeV the relevant decay modes of H_2^+ are: $W^+H_1^0$ in the range $\tan\beta < 1.5$, $W^+H_2^0$ when $1.5 < \tan\beta < 2$, W^+Z^0 for $2 < \tan\beta < 60$. Finally, the dominant mode for the H_3^+ is W^+Z^0 .

IV. DIRECT CHARGED HIGGS PRODUCTION AT THE LHC IN THE MSSM+1CHT

We have found that, in some of the MSSM+1CHT scenarios envisaged here, light charged Higgs bosons could exist that have not been excluded by current experimental bounds, chiefly from LEP2 and Tevatron. Their discovery potential should therefore be studied in view of the upcoming LHC and we shall then turn our attention now to presenting the corresponding hadro-production cross

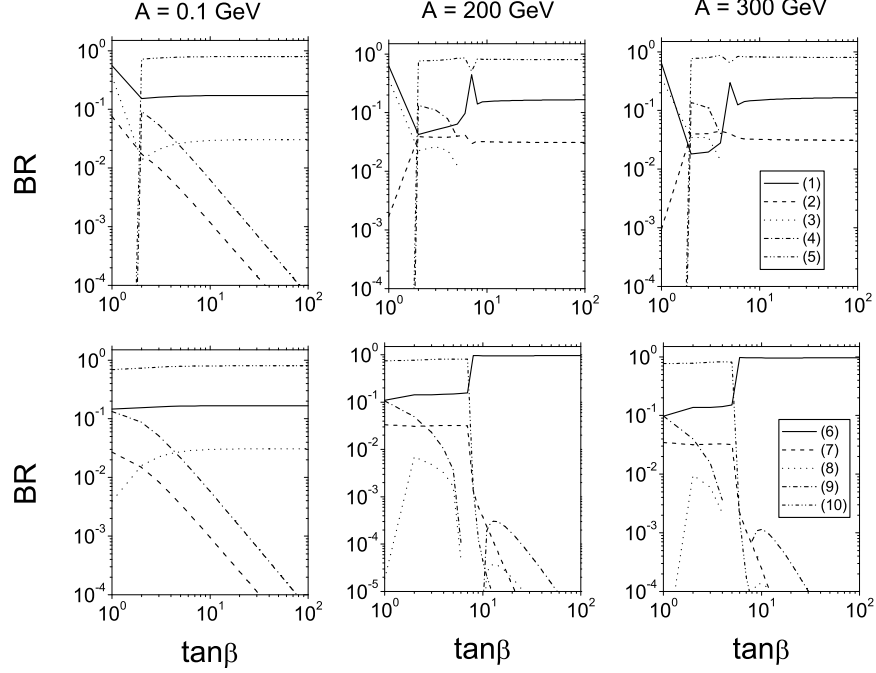


FIG. 32: The figure shows the branching ratios of H_2^+ (top) and H_3^+ (bottom) decaying into the principal modes in Scenario B, with $\lambda = 0.1$ and $\mu_1 = 200$ GeV, for: $A = 0.1$ GeV (left), $A = 200$ GeV (center), $A = 300$ GeV (right). The lines correspond to: (1) $\text{BR}(H_2^+ \rightarrow t\bar{b})$, (2) $\text{BR}(H_2^+ \rightarrow W^+H_1^0)$, (3) $\text{BR}(H_2^+ \rightarrow W^+H_2^0)$, (4) $\text{BR}(H_2^+ \rightarrow W^+A_1^0)$, (5) $\text{BR}(H_2^+ \rightarrow W^+Z^0)$, (6) $\text{BR}(H_3^+ \rightarrow t\bar{b})$, (7) $\text{BR}(H_3^+ \rightarrow W^+H_1^0)$, (8) $\text{BR}(H_3^+ \rightarrow W^+H_2^0)$, (9) $\text{BR}(H_3^+ \rightarrow W^+A_1^0)$, (10) $\text{BR}(H_3^+ \rightarrow W^+Z^0)$.

sections via direct channels, i.e., other than as secondary products in (anti)top quark decays.

As dealt with so far, if the charged Higgs boson mass $m_{H_i^\pm}$ satisfies $m_{H_i^\pm} < m_t - m_b$, where m_t is the top quark mass and m_b the bottom quark mass, H_i^\pm particles could be produced in the decay of on-shell (i.e., $\Gamma_t \rightarrow 0$) top (anti-)quarks $t \rightarrow bH^+$, and the charge conjugated (c.c.) process, the latter being in turn produced in pairs via $q\bar{q}$ annihilation and gg fusion. We denote such a H_i^\pm production channel as $q\bar{q}, gg \rightarrow t\bar{t} \rightarrow t\bar{b}H_i^- + \text{c.c.}$ (i.e., if due to (anti-)top decays) whilst we use the notation $q\bar{q}, gg \rightarrow t\bar{t}H_i^- + \text{c.c.}$ to signify when further production diagrams are included². In fact, owing to the large top decay width ($\Gamma_t \simeq 1.5$ GeV) and due to the additional diagrams which do not proceed via direct $t\bar{t}$ production but yield the same final state $t\bar{b}H_i^- + \text{c.c.}$ [31, 32, 33],

² Altogether, they represent the full gauge invariant set of Feynman graphs pertaining to the $2 \rightarrow 3$ body process with a $t\bar{b}H_i^- + \text{c.c.}$ final state: two for the case of $q\bar{q}$ annihilation and eight for gluon-gluon fusion, see, e.g., Eq. (1.1) of [30].

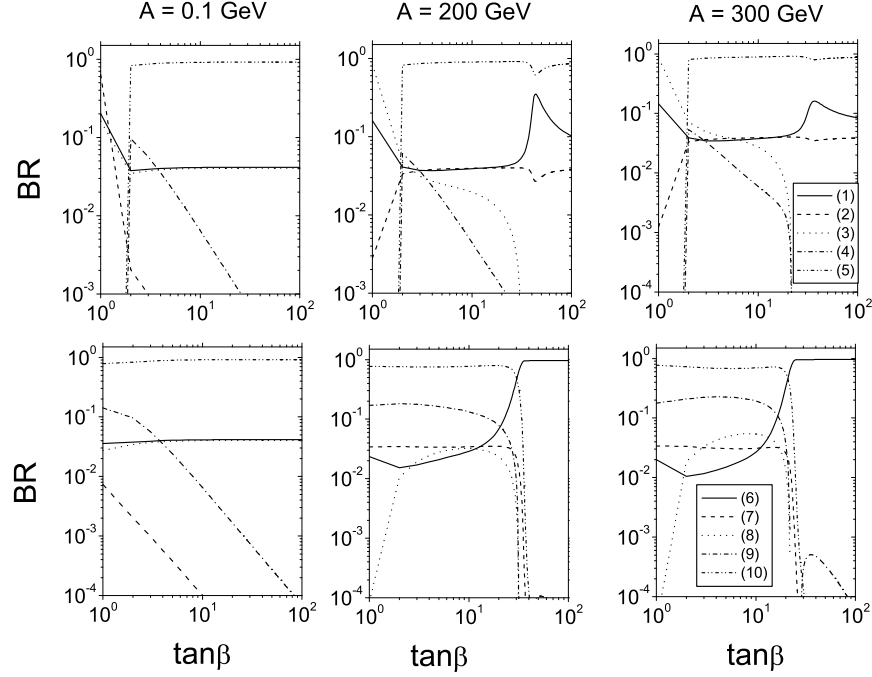


FIG. 33: Same as Figure 32, but taking $\lambda = 0.5$.

charged Higgs bosons could also be produced at and beyond the kinematic top decay threshold. The importance of these effects in the so-called ‘threshold’ or ‘transition’ region ($m_{H_i^\pm} \approx m_t$) was emphasized in various Les Houches proceedings [34, 35] as well as in Refs. [30, 36, 37, 38], so that the calculations of Refs. [31, 32] (based on the appropriate $q\bar{q}, gg \rightarrow tbH_i^\pm$ description) are now implemented in HERWIG [39, 40, 41, 42] and PYTHIA [43, 44]. A comparison between the two generators was carried out in Ref. [36]. For any realistic simulation of H_i^\pm production with $m_{H_i^\pm} \gtrsim m_t$, as can well be the case here, the use of either of these two implementations is of paramount importance.

Here, we use HERWIG version 6.510 in default configuration, by onsetting the subprocess IPROC = 3839, wherein we have overwritten the default MSSM/2HDM couplings and masses with those pertaining to the MSSM+1CHT: see Eqs. (21)–(22). The production cross sections are found in Figures 37–39 and Figures 40–42 for our usual A ($\mu_1 = 0$) and B ($\mu_2 = 0$) Scenarios, respectively, for various different choices of λ and A . (See also Figure 43, illustrating the cross section dependence on $\tan\beta$ for $\lambda = 0.5$, $A = 0$ and $\mu_1 = 200, 400, 700$ GeV.)

The pattern of the H_1^\pm cross sections reflects the usual dependence of the H^\pm state of the MSSM/2HDM, $\sim (m_t^2 \cot^2 \beta + m_b^2 \tan^2 \beta)/(m_t^2 + m_b^2)$, induced by the Yukawa couplings inside the

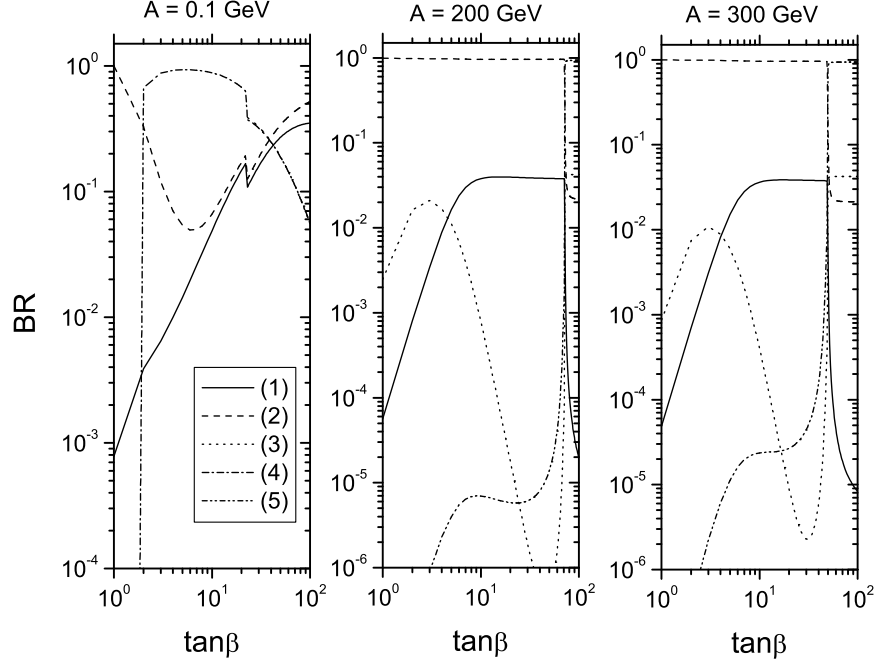


FIG. 34: The figure shows the branching ratios of H_1^\pm decaying into the principal modes in Scenario B, taking $\lambda = 1$ and $\mu_1 = 200$ GeV for: $A = 0.1$ GeV (left), $A = 200$ GeV (center), $A = 300$ GeV (right). The lines correspond to the modes: (1) $\text{BR}(H_1^\pm \rightarrow \tau^\pm \nu_\tau)$, (2) $\text{BR}(H_1^\pm \rightarrow t\bar{b})$, (3) $\text{BR}(H_1^\pm \rightarrow W^\pm H_1^0)$, (4) $\text{BR}(H_1^\pm \rightarrow W^\pm A_1^0)$, (5) $\text{BR}(H_1^\pm \rightarrow W^\pm Z^0)$.

$\bar{t}bH^-$ vertex for the case of the H_1^\pm , with a minimum at $\tan \beta \approx 6$, as seen in Figures 37–39, our Scenario A. (In the last plot, one may appreciate also some peculiar interference effects between the $q\bar{q}, gg \rightarrow t\bar{t} \rightarrow \bar{t}bH_i^- + \text{c.c.}$ diagrams and the remaining ones, modulated by the top width.) The same can be said for the two heavier MSSM+1CHT states, H_2^\pm and H_3^\pm , with the minima shifted to lower $\tan \beta$ values, the more so the heavier the Higgs boson, signalling that are the Yukawa couplings of these last two particles those differing most from the MSSM/2HDM limit. In the case of Scenario B, Figures 40–43, the aforementioned coupling induced dependence upon $\tan \beta$ is only seen for the H_1^\pm state for very small A 's ($A = 0.1$ and $\mu_1 = 200$ GeV or even for $A = 0$ GeV and μ_1 arbitrary). In all other parameter configurations, the H_1^\pm trends differ dramatically from the usual (nearly parabolic) dependence typical of the MSSM/2HDM limit. The same can be said for all setups chosen in the case of the H_2^\pm and H_3^\pm . These peculiar patterns can be understood by using the analytic expressions given in Ref. [10] for the mass spectrum of the charged Higgs bosons

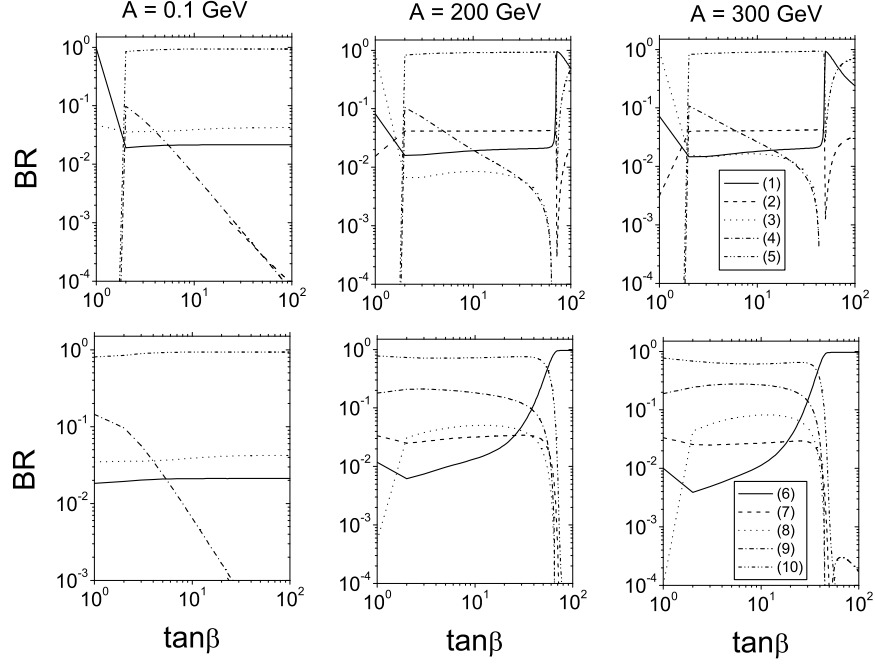


FIG. 35: Same as Figure 32, but taking $\lambda = 1$.

in the approximation $R \ll 1$. In this approximation, we can obtain in Scenario B that:

$$m_{H_3^\pm} \sim 2\mu_1 A / \sin 2\beta,$$

$$m_{H_{1,2}^\pm} \sim \lambda v / (2\sqrt{2}R) (A \sin 2\beta + 2\mu_1) \pm 1/2(g^2 - \lambda^2)v^2. \quad (24)$$

In the range $5 \lesssim \tan \beta \lesssim 100$, $\sin 2\beta$ decreases from ~ 0.1 to ~ 0.01 . This explains the shapes of the curves showed in the Figures 40–42. The parameter λ just determines where the curves for $m_{H_{1,2}^\pm}$ begin to fall. On the other hand, the pattern $(m_t^2 \cot \beta^2 + m_b^2 \tan \beta^2) / (m_t^2 + m_b^2)$ is suppressed by a factor of 10^{-2} for $m_{H_{1,2}^\pm}$ when A and $\tan \beta$ are large.

Altogether, by comparing the $q\bar{q}, gg \rightarrow t\bar{b}H_i^- + \text{c.c.}$ cross sections herein with, e.g., those of the MSSM in [45] or the 2HDM in [37, 46], it is clear that the MSSM+1CHT rates can be very large and thus the discovery potential in ATLAS and CMS can be substantial, particularly for a very light H_1^\pm , which may pertain to our MSSM+1CHT but not the MSSM or general 2HDM. However, it is only by combining the production rates of this section with the decay ones of the previous ones that actual event numbers at the LHC can be predicted.

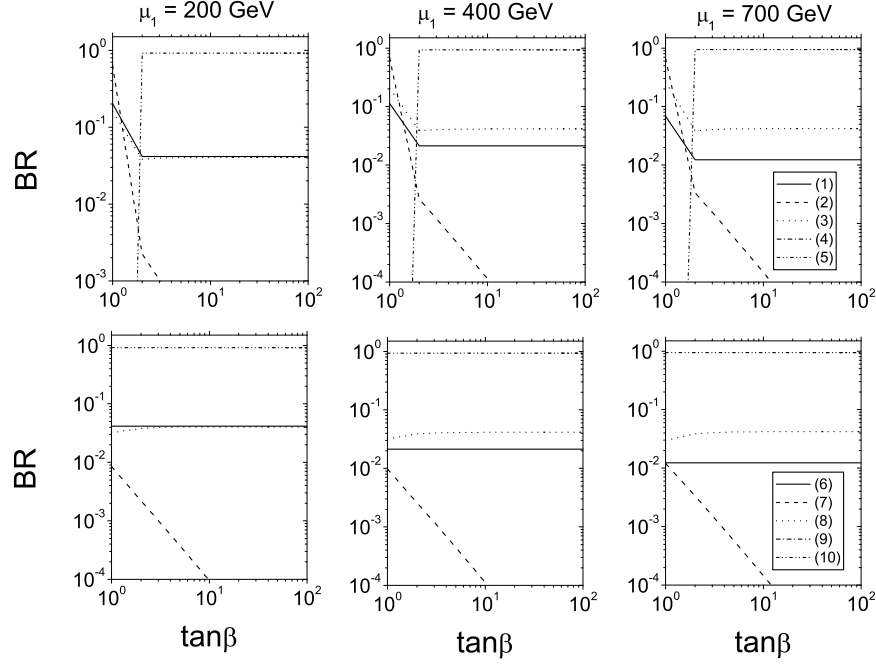


FIG. 36: The figure shows the branching ratios of H_2^+ (top) and H_3^+ (bottom) decaying into the principal modes in Scenario B, taking $\lambda = 0.1$ and $A = 0$ GeV for: $\mu_1 = 200$ GeV (left), $\mu_1 = 400$ GeV (center), $\mu_1 = 700$ GeV (right). The lines correspond to: (1) $\text{BR}(H_2^+ \rightarrow t\bar{b})$, (2) $\text{BR}(H_2^+ \rightarrow W^+ H_1^0)$, (3) $\text{BR}(H_2^+ \rightarrow W^+ H_2^0)$, (4) $\text{BR}(H_2^+ \rightarrow W^+ A_1^0)$, (5) $\text{BR}(H_2^+ \rightarrow W^+ Z^0)$, (6) $\text{BR}(H_3^+ \rightarrow t\bar{b})$, (7) $\text{BR}(H_3^+ \rightarrow W^+ H_1^0)$, (8) $\text{BR}(H_3^+ \rightarrow W^+ H_2^0)$, (9) $\text{BR}(H_3^+ \rightarrow W^+ A_1^0)$, (10) $\text{BR}(H_3^+ \rightarrow W^+ Z^0)$.

V. CHARGED HIGGS BOSON EVENT RATES AT THE LHC IN THE MSSM+1CHT

To illustrate the type of charged Higgs signatures that have the potential to be detectable at the LHC, we show in Tables V and VI a summary of results for masses, LHC cross sections (σ 's), BR's and event rates. We focus on those cases where the charged Higgs boson mass is above the threshold for $t \rightarrow H^\pm b$. Thus, for Scenario A, all the entries for σ 's and BR's in Table V correspond to the second charged Higgs boson H_2^\pm , while for Scenario B, Table VI shows the corresponding results for H_1^\pm . All of these rates correspond to $\mu_2 = 100$ GeV for Scenario A and $\mu_1 = 200$ GeV for Scenario B. The cases where $t \rightarrow H_i^\pm b$ is allowed have been discussed previously in section III. We shall also assume an integrated luminosity of 10^{-5} pb^{-1} .

To illustrate these results, let us comment one case within each scenario. From Table V, we can see that for Scenario A, with $\lambda = 0.5$, $A = 200$ GeV and $\tan \beta = 20$, we have that H_2^+ is heavier than $m_t - m_b$, with a mass $m_{H_2^+} = 390$ GeV, this precluding top decay contributions, so that in this case

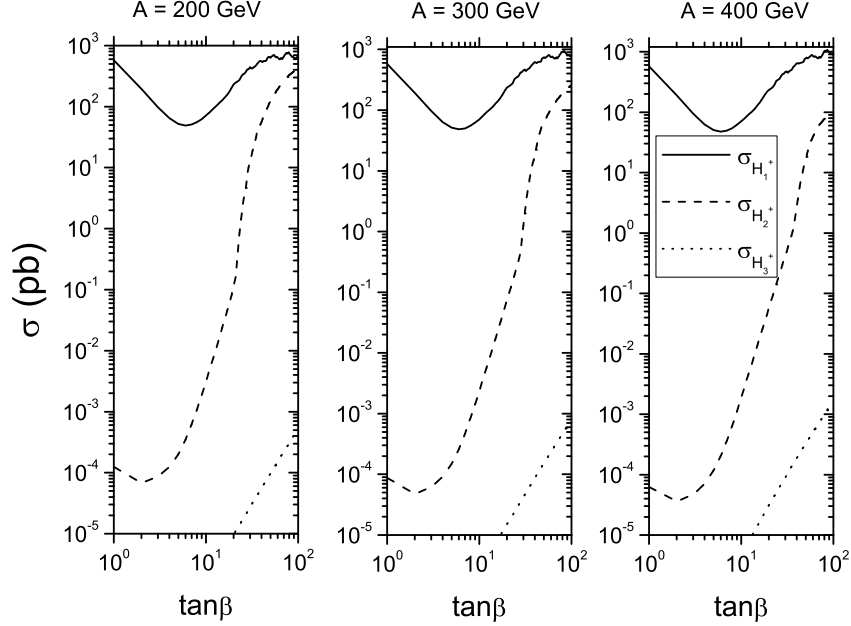


FIG. 37: The figure shows the cross sections of $H_{1,2,3}^+$ at the LHC through the channel $q\bar{q}, gg \rightarrow t\bar{b}H^- + \text{c.c.}$ in Scenario A with $\lambda = 0.1$ and for: $A = 200, 300, 400$ GeV, respectively.

$\sigma(pp \rightarrow t\bar{b}H^+) \approx 1.2 \times 10^{-2}$ pb, while the dominant decays are $H_2^+ \rightarrow t\bar{b}, W^+A_1^0, W^+Z^0, W^+H_1^0$ which give a number of events of 180, 900, 12, 92, respectively. In this case the most promising signal is $H_2^+ \rightarrow W^+A_1^0$. However, when $\lambda = 1.0$ we have that all event rates get decreased, partially because the masses get enhanced. For instance $m_{H_2^+}$ becomes 545 GeV, however the number of events at the LHC for $H_2^+ \rightarrow W^+A_1^0$ can still be substantial, as it is about 349.

Then, for Scenario B, we have that H_1^+ is already above the threshold for $t \rightarrow H_i^+b$. So, for the declared values of the relevant parameters, we obtain that the lightest charged Higgs boson mass is $m_{H_1^+} = 906$ and 921 GeV for $\lambda = 0.5$ and $\lambda = 1.0$, respectively. In such a case only the decay $H_1^+ \rightarrow t\bar{b}$ can reach significant numbers for the LHC. We obtain a number of events of 912 and 854, respectively. The other decay that has a large BR is $H_1^+ \rightarrow \tau^+\nu_\tau$, but in all cases the number of events is at most of order 20–30, which seems quite difficult to be detectable at the CERN machine.

Thus, we conclude that signatures in Scenario A are more diverse than for Scenario B. However, in order to reach quantitative conclusions we need to perform a study of signal *versus* background, but this seems more tractable if we concentrate in each mode individually, rather than while taking the general view that was attempted in this paper.

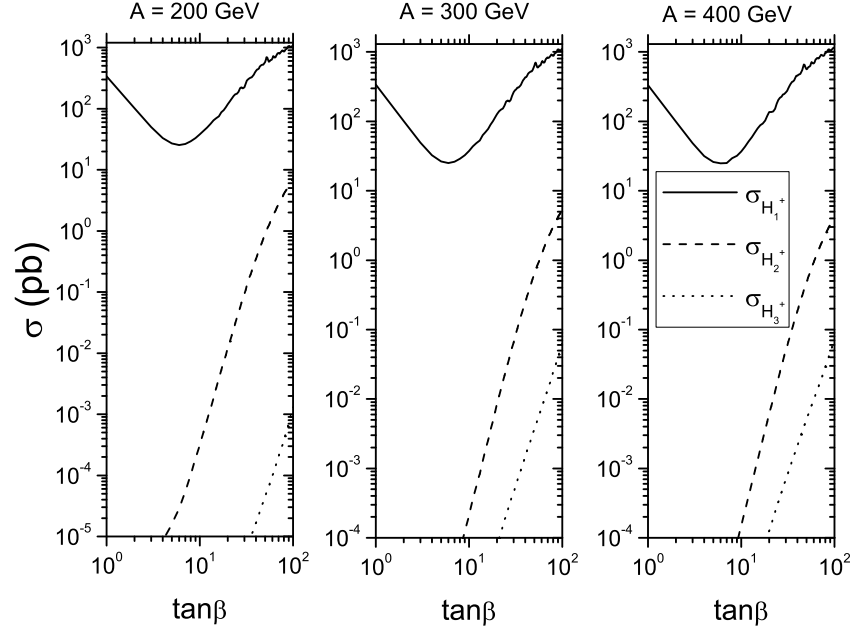


FIG. 38: The figure shows the cross sections of $H_{1,2,3}^+$ at the LHC through the channel $q\bar{q}, gg \rightarrow t\bar{b}H^- + \text{c.c.}$ in Scenario A with $\lambda = 0.5$ and for: $A = 200, 300, 400$ GeV, respectively.

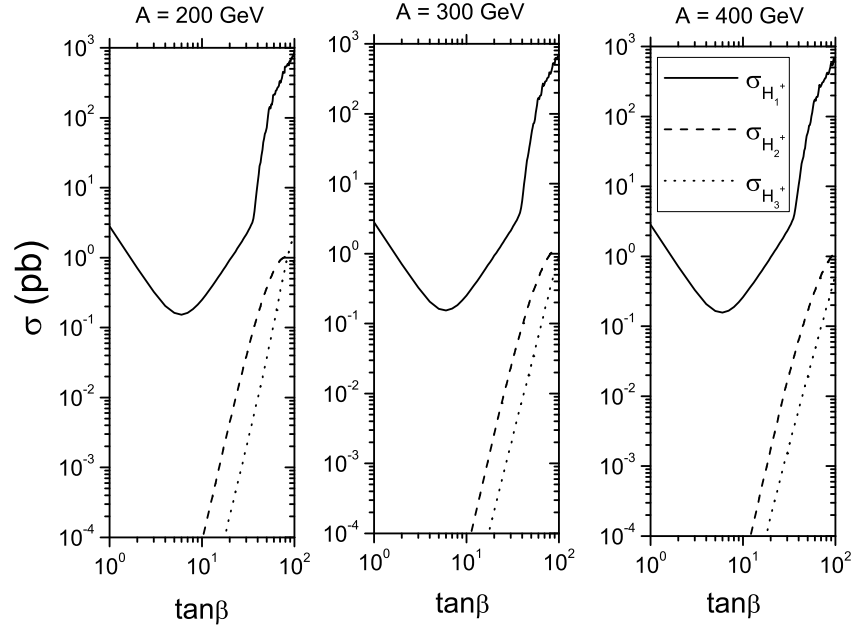


FIG. 39: The figure shows the cross sections of $H_{1,2,3}^+$ at the LHC through the channel $q\bar{q}, gg \rightarrow t\bar{b}H^- + \text{c.c.}$ in Scenario A with $\lambda = 1.0$ and for: $A = 200, 300, 400$ GeV, respectively.

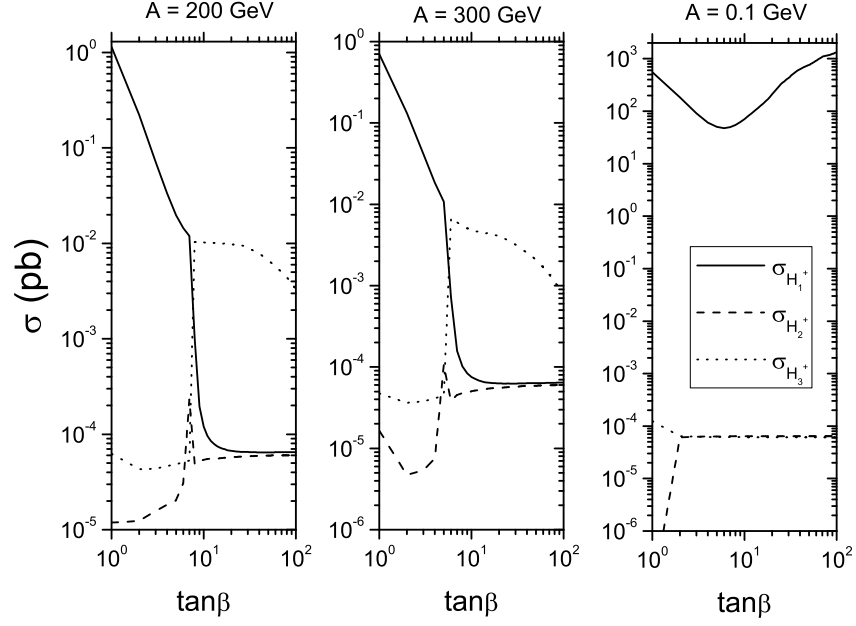


FIG. 40: The figure shows the cross sections of $H_{1,2,3}^+$ at the LHC through the channel $q\bar{q}, gg \rightarrow t\bar{b}H^- + \text{c.c.}$ in Scenario B with $\lambda = 0.1$ and for: $A = 200, 300, 0.1$ GeV, respectively.

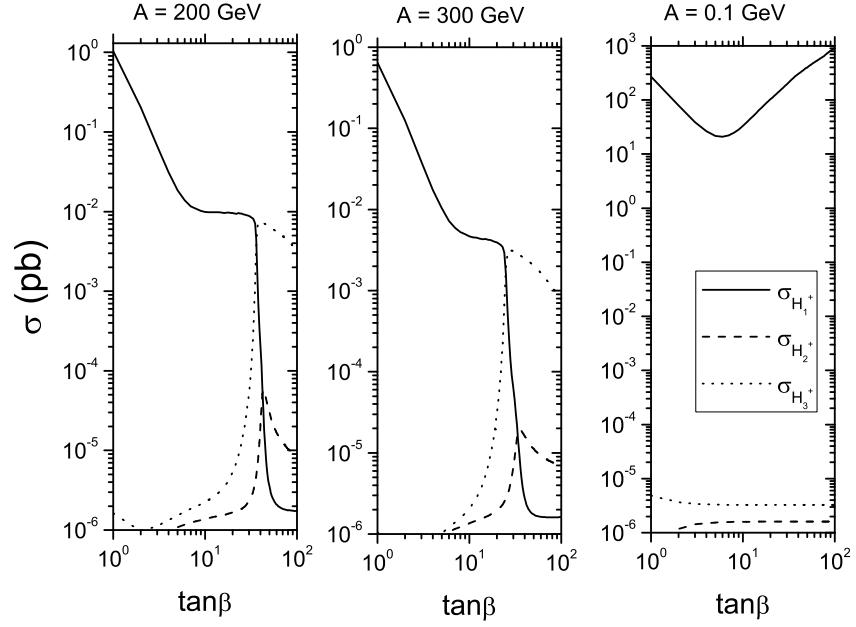


FIG. 41: The figure shows the cross sections of $H_{1,2,3}^+$ at the LHC through the channel $q\bar{q}, gg \rightarrow t\bar{b}H^- + \text{c.c.}$ in Scenario B with $\lambda = 0.5$ and for: $A = 200, 300, 0.1$ GeV, respectively.

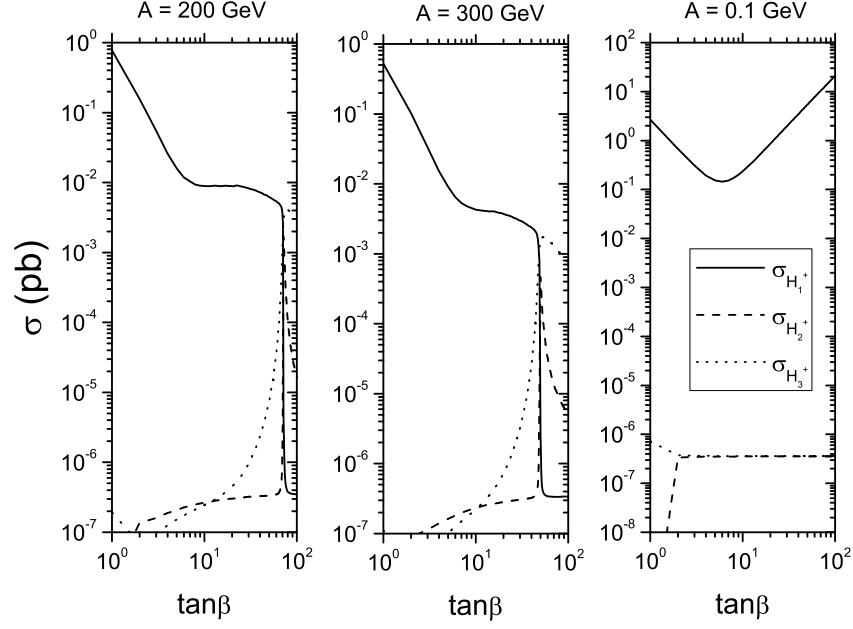


FIG. 42: The figure shows the cross sections of $H_{1,2,3}^+$ at the LHC through the channel $q\bar{q}, gg \rightarrow t\bar{b}H^- + \text{c.c.}$ in Scenario B with $\lambda = 1.0$ and for: $A = 200, 300, 0.1$ GeV, respectively.

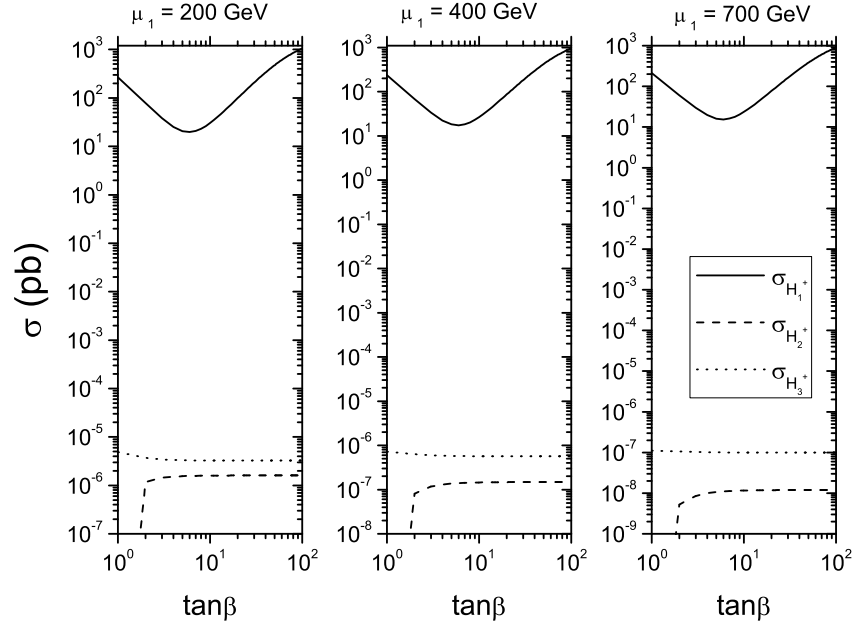


FIG. 43: The figure shows the cross sections of $H_{1,2,3}^+$ at the LHC through the channel $q\bar{q}, gg \rightarrow t\bar{b}H^- + \text{c.c.}$ in Scenario B with $A = 0$ GeV, $\lambda = 0.5$ and for: $\mu_1 = 200, 400, 700$ GeV, respectively.

VI. CONCLUSIONS

After describing the entire Higgs mass and coupling spectrum, we have studied the fermion-charged Higgs bosons vertices within the context of an extension of the Minimal Supersymmetric Standard Model with an additional Complex Higgs Triplet (MSSM+1CHT). Then we have analyzed the decay $t \rightarrow b H_i^+$ ($i = 1, 2, 3$.) in the framework of this model. We have found that in some plausible scenarios of the MSSM+1CHT the experimental data allow regions in the plane $M_{H_i^\pm} - \tan\beta$ for the lightest charged Higgs boson H_1^\pm (even for H_2^\pm) that are forbidden in the case of the MSSM. For instance, in this model it is possible to have a charged Higgs boson with mass $m_{H^\pm} \approx m_{W^\pm}$ which is not excluded yet by any of the current data. Furthermore, there are other regions of parameters where the top quark can decay into two charged Higgs states, so that plenty of these states could be produced at the LHC in (anti)top quark decays. Whenever the mass of the charged Higgs boson is larger than m_t , there is scope to exploit direct H_i^\pm hadro-production through the associate mode $q\bar{q}, gg \rightarrow t\bar{b}H_i^- + \text{c.c.}$

On the one hand, the detection at the LHC of charged Higgs bosons in the regions of parameter space accessible in the MSSM (or a 2HDM) would not contradict the MSSM+1CHT hypothesis. On the other hand, the observation at such a machine of several charged Higgs bosons would correspond to a model with a more elaborate Higgs sector than the MSSM (or a 2HDM), such as the MSSM+1CHT.

Acknowledgements: This work was supported by CONACyT and SNI (México). J.H.S. thanks in particular CONACyT (México) for the grant J50027-F. S.M. acknowledges the FP6 RTN MRTN-CT-2006-035505 (HEPTOOLS, Tools and Precision Calculations for Physics Discoveries at Colliders) for partial support and The Royal Society (London, UK) for a Conference Grant to attend the meeting ‘Charged2006’, where this work was started.

TABLE V: Summary of LHC event rates for Scenario A with $\mu_2 = 100$ GeV for an integrated luminosity of 10^5 pb^{-1} , for several different signatures.

λ	$(A, \tan \beta)$	$m_{H_1^+}$ in GeV	$\sigma(pp \rightarrow H_2^+ tb)$ in pb	Relevant BR's	Nr. Events
0.5	(200,5)	(118,740,790)	1.6×10^{-5}	$\text{BR}(H_2^+ \rightarrow tb) \approx 5.8 \times 10^{-4}$	0
				$\text{BR}(H_2^+ \rightarrow W^+ A_1^0) \approx 9.8 \times 10^{-1}$	1
				$\text{BR}(H_2^+ \rightarrow W^+ Z^0) \approx 1.2 \times 10^{-2}$	0
				$\text{BR}(H_2^+ \rightarrow W^+ H_1^0) \approx 4.2 \times 10^{-3}$	0
0.5	(200,20)	(114,390,470)	1.2×10^{-2}	$\text{BR}(H_2^+ \rightarrow tb) \approx 1.5 \times 10^{-1}$	180
				$\text{BR}(H_2^+ \rightarrow W^+ A_1^0) \approx 7.5 \times 10^{-1}$	900
				$\text{BR}(H_2^+ \rightarrow W^+ Z^0) \approx 1.0 \times 10^{-2}$	12
				$\text{BR}(H_2^+ \rightarrow W^+ H_1^0) \approx 7.7 \times 10^{-2}$	92
0.5	(200,50)	(98,290,370)	8.7×10^{-1}	$\text{BR}(H_2^+ \rightarrow \tau^+ \nu_\tau) \approx 8.2 \times 10^{-2}$	7134
				$\text{BR}(H_2^+ \rightarrow tb) \approx 8.4 \times 10^{-1}$	73080
				$\text{BR}(H_2^+ \rightarrow W^+ A_1^0) \approx 2.4 \times 10^{-2}$	2088
				$\text{BR}(H_2^+ \rightarrow W^+ H_1^0) \approx 4.8 \times 10^{-2}$	4176
1.0	(200,5)	(191,1047,1087)	3.4×10^{-6}	$\text{BR}(H_2^+ \rightarrow \tau^+ \nu_\tau) \approx 4.6 \times 10^{-6}$	0
				$\text{BR}(H_2^+ \rightarrow tb) \approx 3.0 \times 10^{-4}$	0
				$\text{BR}(H_2^+ \rightarrow W^+ A_1^0) \approx 9.8 \times 10^{-1}$	0
				$\text{BR}(H_2^+ \rightarrow W^+ Z^0) \approx 1.3 \times 10^{-2}$	0
1.0	(200,20)	(185,545,610)	4.5×10^{-3}	$\text{BR}(H_2^+ \rightarrow tb) \approx 1.1 \times 10^{-1}$	50
				$\text{BR}(H_2^+ \rightarrow W^+ A_1^0) \approx 7.7 \times 10^{-1}$	349
				$\text{BR}(H_2^+ \rightarrow W^+ Z^0) \approx 1.1 \times 10^{-2}$	5
				$\text{BR}(H_2^+ \rightarrow W^+ H_1^0) \approx 1.0 \times 10^{-2}$	4
1.0	(200,50)	(153,400,450)	3.6×10^{-1}	$\text{BR}(H_2^+ \rightarrow \tau^+ \nu_\tau) \approx 5.0 \times 10^{-2}$	1800
				$\text{BR}(H_2^+ \rightarrow tb) \approx 8.4 \times 10^{-1}$	30240
				$\text{BR}(H_2^+ \rightarrow W^+ A_1^0) \approx 2.6 \times 10^{-2}$	936
				$\text{BR}(H_2^+ \rightarrow W^+ H_1^0) \approx 7.9 \times 10^{-2}$	2844

TABLE VI: Summary of LHC event rates for Scenario B with $\mu_1 = 200$ GeV for an integrated luminosity of 10^5 pb^{-1} , for several different signatures.

λ	$(A, \tan \beta)$	$m_{H_1^+}$ in GeV	$\sigma(pp \rightarrow H_1^+ tb)$ in pb	Relevant BR's	Nr. Events
0.5	(200,5)	(473,1304,1305)	1.8×10^{-2}	$\text{BR}(H_1^+ \rightarrow \tau^+ \nu_\tau) \approx 1.7 \times 10^{-2}$	31
				$\text{BR}(H_1^+ \rightarrow tb) \approx 9.8 \times 10^{-1}$	1764
				$\text{BR}(H_1^+ \rightarrow W^+ Z^0) \approx 4.2 \times 10^{-6}$	0
				$\text{BR}(H_1^+ \rightarrow W^+ H_1^0) \approx 5.4 \times 10^{-4}$	1
0.5	(200,20)	(906,1223,1225)	9.6×10^{-3}	$\text{BR}(H_1^+ \rightarrow \tau^+ \nu_\tau) \approx 3.9 \times 10^{-2}$	37
				$\text{BR}(H_1^+ \rightarrow tb) \approx 9.5 \times 10^{-1}$	912
				$\text{BR}(H_1^+ \rightarrow W^+ Z^0) \approx 1.4 \times 10^{-5}$	0
				$\text{BR}(H_1^+ \rightarrow W^+ H_1^0) \approx 2.1 \times 10^{-6}$	0
0.5	(200,50)	(1206,1207,1424)	2.0×10^{-6}	$\text{BR}(H_1^+ \rightarrow \tau^+ \nu_\tau) \approx 3.8 \times 10^{-3}$	0
				$\text{BR}(H_1^+ \rightarrow tb) \approx 1.3 \times 10^{-1}$	0
				$\text{BR}(H_1^+ \rightarrow W^+ Z^0) \approx 8.3 \times 10^{-1}$	0
				$\text{BR}(H_1^+ \rightarrow W^+ H_1^0) \approx 3.6 \times 10^{-2}$	0
1.0	(200,5)	(497,1838,1850)	1.6×10^{-2}	$\text{BR}(H_1^+ \rightarrow \tau^+ \nu_\tau) \approx 1.6 \times 10^{-2}$	26
				$\text{BR}(H_1^+ \rightarrow tb) \approx 9.7 \times 10^{-1}$	1552
				$\text{BR}(H_1^+ \rightarrow W^+ Z^0) \approx 4.0 \times 10^{-6}$	0
				$\text{BR}(H_1^+ \rightarrow W^+ H_1^0) \approx 1.1 \times 10^{-2}$	18
1.0	(200,20)	(921,1724,1738)	8.9×10^{-3}	$\text{BR}(H_1^+ \rightarrow \tau^+ \nu_\tau) \approx 3.9 \times 10^{-2}$	35
				$\text{BR}(H_1^+ \rightarrow tb) \approx 9.6 \times 10^{-1}$	854
				$\text{BR}(H_1^+ \rightarrow W^+ Z^0) \approx 5.8 \times 10^{-6}$	0
				$\text{BR}(H_1^+ \rightarrow W^+ H_1^0) \approx 1.8 \times 10^{-5}$	0
1.0	(200,50)	(1434,1699,1713)	6.2×10^{-3}	$\text{BR}(H_1^+ \rightarrow \tau^+ \nu_\tau) \approx 3.8 \times 10^{-2}$	24
				$\text{BR}(H_1^+ \rightarrow tb) \approx 9.6 \times 10^{-1}$	595
				$\text{BR}(H_1^+ \rightarrow W^+ Z^0) \approx 1.4 \times 10^{-5}$	0
				$\text{BR}(H_1^+ \rightarrow W^+ H_1^0) \approx 5.8 \times 10^{-7}$	0

-
- [1] S. L. Glashow, Nucl. Phys. **22**, 579 (1961); S. Weinberg, Phys. Rev. Lett. **19**, 1264 (1967); A. Salam, Proc. 8th NOBEL Symposium, ed. N. Svartholm (Almqvist and Wiksell, Stockholm, 1968), p. 367.
 - [2] S. Dawson et al., *The Higgs Hunter's Guide*, 2nd ed., Frontiers in Physics Vol. **80** (Addison-Wesley, Reading MA, 1990).
 - [3] For a review of SM and MSSM Higgs Physics at the LHC see, e.g.: A. Djouadi, hep-ph/0503172 and hep-ph/0503173.
 - [4] M. Carena *et al.*, hep-ph/0010338; C. Balazs *et al.*, Phys. Rev. **D59**, 055016 (1999); J. L. Díaz-Cruz *et al.*, Phys. Rev. Lett. **80**, 4641 (1998).
 - [5] See, e.g., recent work on Little Higgs models: N. Arkani-Hamed, A. G. Cohen, E. Katz and A. E. Nelson, JHEP **0207**, 034 (2002). And on AdS/CFT Higgs models: R. Contino, Y. Nomura and A. Pomarol, Nucl. Phys. B **671**, 148 (2003); A. Aranda, J. L. Diaz-Cruz, J. Hernandez-Sanchez and R. Noriega-Papaqui, 0708.3821 [hep-ph].
 - [6] T. G. Rizzo, Mod. Phys. Lett. A **6**, 1961 (1991).
 - [7] J. W. F. Valle, hep-ph/0608101; S. Kanemura, T. Kasai, G. L. Lin, Y. Okada, J. J. Tseng and C. P. Yuan, Phys. Rev. D **64**, 053007 (2001).
 - [8] A. Aranda, C. Balazs and J. L. Diaz-Cruz, Nucl. Phys. B **670**, 90 (2003); A. Aranda and J. L. Diaz-Cruz, Phys. Lett. B **633**, 591 (2006).
 - [9] J. F. Gunion, R. Vega and J. Wudka, Phys. Rev. D **42**, 1673 (1990).
 - [10] J. R. Espinosa and M. Quiros, Nucl. Phys. B **384**, 113 (1992).
 - [11] O. Felix-Beltran, Int. J. Mod. Phys. A **17**, 465 (2002).
 - [12] S. Moretti and W. J. Stirling, Phys. Lett. B **347**, 291 (1995) [Erratum-ibid. B **366**, 451 (1996)]; A. Djouadi, J. Kalinowski and P. M. Zerwas, Z. Phys. C **70**, 435 (1996).
 - [13] J. L. Díaz-Cruz and M.A. Pérez, Phys. Rev. **D33**, 273 (1986); J.F. Gunion, G.L. Kane and J. Wudka, Nucl. Phys. **B299**, 231 (1988); A. Mendez and A. Pomarol, Nucl. Phys. **B349**, 369 (1991); E. Baradas *et al.*, Phys. Rev. **D53**, 1678 (1996); M. Capdequi-Peyranere, H. E. Haber, and P. Iruelgui, Phys. Rev. **D44**, 191 (1991); S. Kanemura, Phys. Rev. **D61**, 095001 (2000); K.A. Assamagan *et al.*, hep-ph/0406152; J. Hernández-Sánchez *et al.*, Phys. Rev. **D69**, 095008 (2004).
 - [14] M. Bisset, M. Guchait and S. Moretti, Eur. Phys. J. C **19**, 143 (2001); M. Bisset, F. Moortgat and S. Moretti, Eur. Phys. J. C **30**, 419 (2003).
 - [15] J. L. Díaz-Cruz, J. Hernández-Sánchez and J.J. Toscano, Phys. Lett. **B512**, 339 (2001).
 - [16] E. Barradas-Guevara, O. Félix-Beltrán, J. Hernández-Sánchez and A. Rosado, Phys. Rev. D **71**, 073004 (2005).
 - [17] K. A. Assamagan, J. Guasch, S. Moretti and S. Penaranda, hep-ph/0402212; K. A. Assamagan, J. Guasch, S. Moretti and S. Penaranda, Czech. J. Phys. **55**, B787 (2005).
 - [18] J. L. Díaz-Cruz and O. A. Sampayo, Phys. Rev. **D50**, 6820 (1994); J.F. Gunion *et al.*, Nucl. Phys.

- B294**, 621 (1987); M. A. Pérez and A. Rosado, Phys. Rev. **D30**, 228 (1984).
- [19] S. Moretti and K. Odagiri, Phys. Rev. D **55**, 5627 (1997); F. Borzumati, J.-L. Kneur and N. Polonsky, Phys. Rev. D **60**, 115011 (1999); D.J. Miller, S. Moretti, D.P. Roy and W.J. Stirling, Phys. Rev. **D61**, 055011 (2000); S. Moretti and D. P. Roy, Phys. Lett. B **470**, 209 (1999); A. A. Barrientos Bendezu and B. A. Kniehl, Phys. Rev. D **59**, 015009 (1999), Phys. Rev. D **61**, 097701 (2000) and Phys. Rev. D **63**, 015009 (2001); O. Brein, W. Hollik and S. Kanemura, Phys. Rev. D **63**, 095001 (2001) [arXiv:hep-ph/0008308]; A. Belyaev, D. Garcia, J. Guasch and J. Sola, JHEP **0206**, 059 (2002) and Phys. Rev. D **65**, 031701 (2002).
 - [20] S. H. Zhu, Phys. Rev. D **67**, 075006 (2003); T. Plehn, Phys. Rev. D **67**, 014018 (2003); E. L. Berger, T. Han, J. Jiang and T. Plehn, Phys. Rev. D **71**, 115012 (2005).
 - [21] A. Abulencia *et al.* [CDF Collaboration], Phys. Rev. Lett. **96**, 042003 (2006).
 - [22] For a review see: F. Borzumati and A. Djouadi, Phys. Lett. **B549**, 170 (2002); D. P. Roy, Mod. Phys. Lett. **A19**, 1813 (2004).
 - [23] S. Eidelman *et al.* [Particle Data Group], Phys. Lett. B **592**, 1 (2004).
 - [24] J. R. Ellis, G. Ridolfi and F. Zwirner, Phys. Lett. B **257**, 83 (1991) and Phys. Lett. B **262**, 477 (1991).
 - [25] J. R. Espinosa and M. Quirós, Phys. Rev. Lett. **81**, 516 (1998), Phys. Lett. B **302**, 51 (1993) and Phys. Lett. B **279**, 92 (1992).
 - [26] J. L. Díaz-Cruz, J. Hernández-Sánchez, S. Moretti and A. Rosado, in preparation.
 - [27] S. Schael *et al.* [ALEPH Collaboration, DELPHI Collaboration, L3 Collaboration, OPAL Collaborations and LEP Working Group for Higgs Boson Searches], Eur. Phys. J. **C47**, 547 (2006).
 - [28] M. Carena, D. Garcia, U. Nierste and C. E. M. Wagner, Nucl. Phys. B **577**, 88 (2000).
 - [29] [LEP Higgs Working Group for Higgs boson searches], hep-ex/0107031; A. Heister *et al.* [ALEPH Collaboration], Phys. Lett. B **543**, 1 (2002).
 - [30] M. Guchait and S. Moretti, JHEP **0201**, 001 (2002).
 - [31] F. Borzumati, J.-L. Kneur and N. Polonsky, in Ref. [19].
 - [32] D.J. Miller, S. Moretti, D.P. Roy and W.J. Stirling, in Ref. [19].
 - [33] S. Moretti and D. P. Roy, in Ref. [19].
 - [34] D. Cavalli *et al.*, hep-ph/0203056.
 - [35] K. A. Assamagan *et al.*, in Ref. [13].
 - [36] J. Alwall, C. Biscarat, S. Moretti, J. Rathsmann and A. Sopczak, Eur. Phys. J. C **39S1**, 37 (2005).
 - [37] S. Moretti, Pramana **60**, 369 (2003).
 - [38] K. A. Assamagan, M. Guchait and S. Moretti, hep-ph/0402057.
 - [39] G. Abbiendi, I. G. Knowles, G. Marchesini, M. H. Seymour, L. Stanco and B. R. Webber, Comp. Phys. Commun. **67**, 465 (1992).
 - [40] G. Corcella *et al.*, JHEP **0101**, 010 (2001).
 - [41] G. Corcella *et al.*, hep-ph/0210213.
 - [42] S. Moretti, K. Odagiri, P. Richardson, M. H. Seymour and B. R. Webber, JHEP **0204**, 028 (2002).

- [43] T. Sjöstrand, *Comp. Phys. Comm.* **82**, 74 (1994); T. Sjöstrand, P. Edén, C. Friberg, L. Lönnblad, G. Miu, S. Mrenna and E. Norrbin, *Comp. Phys. Commun.* **135**, 238 (2001); T. Sjöstrand, L. Lönnblad and S. Mrenna, hep-ph/0108264; T. Sjöstrand, L. Lönnblad, S. Mrenna and P. Skands, hep-ph/0308153.
- [44] J. Alwall and J. Rathsman, *JHEP* **0412**, 050 (2004).
- [45] A. Djouadi, second paper in [3].
- [46] S. Moretti, *J. Phys. G* **28**, 2567 (2002).